geosciences

MDPI

Article

Deformation of the European Plate (58-0 Ma): Evidence from Calcite Twinning Strains

John P. Craddock [1,*], Uwe Ring [2] and O. Adrian Pfiffner [3]

[1] Geology Department, Macalester College, St. Paul, MN 55105, USA
[2] Institutionen för Geologiska Vetenskaper, Stockholms Universitet, 106 91 Stockholm, Sweden; uwe.ring@geo.su.se
[3] Geologisches Institut, Universitat Bern, 3012 Bern, Switzerland; adrian.pfiffner@geo.unibe.ch
* Correspondence: craddock.irnp@gmail.com

Abstract: We present a data set of calcite twinning strain results (n = 209 samples; 9919 measured calcite twins) from the internal Alpine nappes northwestward across the Alps and Alpine foreland to the older extensional margin along the Atlantic coast in Ireland. Along the coast of Northern Ireland, Cretaceous chalks and Tertiary basalts are cross-cut by calcite veins and offset by calcite-filled normal and strike-slip faults. Both Irish sample suites (n = 16 with four U-Pb vein calcite ages between 70–42 Ma) record a sub-horizontal SW-NE shortening strain with vertical extension and no strain overprint. This sub-horizontal shortening is parallel to the margin of the opening of the Atlantic Ocean (~58 Ma), and this penetrative fabric is only observed ~100 km inboard of the margin to the southeast. The younger, collisional Alpine orogen (~40 Ma) imparted a stress–strain regime dominated by SE-NW sub-horizontal shortening ~1200 km northwest from the Alps preserved in Mesozoic limestones and calcite veins (n = 32) in France, Germany and Britain. This layer-parallel shortening strain (−3.4%, 5% negative expected values) is preserved across the foreland in the plane of Alpine thrust shortening (SE-NW) along with numerous outcrop-scale contractional structures (i.e., folds, thrust faults). Calcite veins were observed in the Alpine foreland in numerous orientations and include both a SE-NW layer-parallel shortening fabric (n = 11) and a sub-vertical NE-SW vein-parallel shortening fabric (n = 4). Alpine foreland strains are compared with twinning strains from the frontal Jura Mountains (n = 9; layer-parallel shortening), the Molasse basin (n = 26; layer-parallel and layer-normal shortening), Pre-Alp nappes (n = 39; layer-parallel and layer-normal shortening), Helvetic and Penninic nappes (Penninic klippe; n = 46; layer-parallel and layer-normal shortening plus four striated U-Pb calcite vein ages ~24 Ma) and calcsilicates from the internal Tauern window (n = 4; layer-normal shortening). We provide a chronology of the stress–strain history of the European plate from 58 Ma through the Alpine orogen.

Keywords: structural geology; calcite strains; thrust belt evolution

Citation: Craddock, J.P.; Ring, U.; Pfiffner, O.A. Deformation of the European Plate (58-0 Ma): Evidence from Calcite Twinning Strains. *Geosciences* **2022**, *12*, 254. https://doi.org/10.3390/geosciences12060254

Academic Editors: Olivier Lacombe and Jesus Martinez-Frias

Received: 23 March 2022
Accepted: 7 June 2022
Published: 20 June 2022

1. Introduction

Orogenic belts generally bury the adjacent foreland in synorogenic debris, making it difficult to study thrust-related deformation inboard of the orogen. Chinn and Konig [1] were the first to measure mechanical twins in calcite in a foreland setting and ponder the origin of this 'far-field' deformation ~100 km north of the Appalachian–Ouachita front in Arkansas, USA. Other finite strain observations in foreland settings [2–5] have confirmed the extent of thrust deformation inboard of the margin and thrust front ("toe"), and distal extent of this deformation was characterized by Craddock and van der Pluijm [6] ~2000 km into the Appalachian foreland and by Lacombe et al. [7] <100 km into the Burgundy region of the Alpine foreland (see also [8–10]). The collective effort of foreland strain studies increased the horizontal dimensions of a critically tapered sedimentary prism that evolves into a thrust belt [11–14] and also provides a pre-thrusting layer-parallel shortening (LPS)

strain fabric that can be used as a passive strain marker in the allochthonous sediments of the adjacent thrust belt. In the collisional Appalachians, all the shortening axes are parallel to thrust motion (SE-NW), identical to the LPS fabric in the allochthonous foreland, so thrust motions did not involve rotation ([15–17], and references therein). In a tectonic setting of oblique convergence, as in the Sevier–Laramide belt, counterclockwise thrust sheet motions are documented when compared to the autochthonous E-W LPS fabric in the foreland [18–20]. The Alps present a collisional mountain belt that is curved (oroclinal), composed of high-grade nappes in its core (hinterland: [21–24]) that overthrust dated synorogenic sediments (molasse and flysch; [23,25–28]) and folded the foreland in amplitudes that diminish NW into the craton (Figure 1; Jura folds vs. the Paris basin; [29]). The influence of far-field stresses decreases into the foreland as a function of the plate boundary type, and it is dependent on whether the boundary is obliquely convergent or collisional and the slab dip that generated the stress field [30–34].

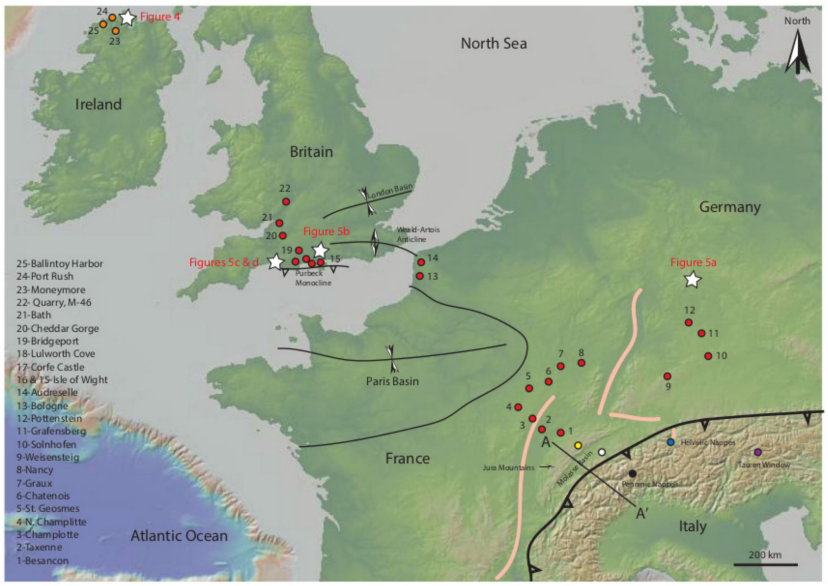

Figure 1. Topographic map of western Europe with regional geologic features related to Alps and the Alpine foreland, including extensional features of the European Central Rift System (ECRIS). Sample sites are listed (left column; red dots, for the foreland, the Alps (many colors, see Figures 2 and 3) and the Irish Coast (orange dots). Locations of field photos in additional figures are indicated by white stars.

In this reconnaissance study (Figure 1), we sampled calcsilicates in the European continental crust in the Tauern window in the eastern Alps (Austria) and Mesozoic carbonates and calcite veins across the Alpine foreland from the Jura Mountains to southwestern Britain, as well as in Northern Ireland, where Cretaceous chalks are offset by normal faults with striated calcite and intruded or overlain by Tertiary basalts with calcite veins [35]. We analyzed the twinned calcite in this suite and compared our results with twinning strain and fabric studies obtained within the Alpine orogen: the Jura folds, [36,37], the Molasse basin, [36,38], the Pre-Alpine nappes [39], the Helvetic nappes [40–42] and the Helvetic–Penninic nappes [40,43]. With this robust data set, we hope to (1) interpret the variations in stress–strain response of the oroclinal Tertiary Alpine orogen across the region into the gently warped foreland (i.e., Paris basin, Purbeck thrust-monocline, London basin, etc.) toward a better understanding of thrust mechanics and (2) couple the twinning strain results associated with Pre-Alpine intra-plate deformation [44–46] and the opening of the North Atlantic (58 Ma), Tertiary Alpine deformation and the modern Icelandic margin [47].

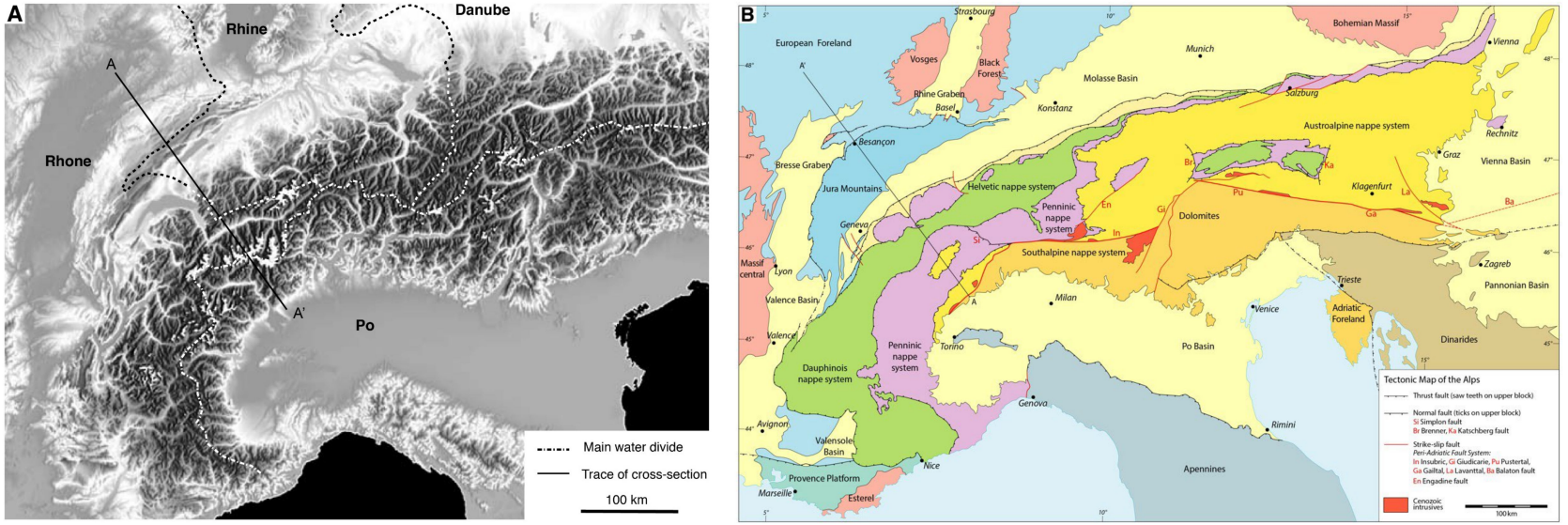

Figure 2. Regional maps of the Alps with cross section line A-A′ shown in Figure 3. (**A**) Digital elevation model with the main drainage divides delimiting the hydrographic basins of the Rhine, Po and Danube rivers. (**B**) Tectonic map of the Alps and their foreland showing the main nappe systems and foreland basins.

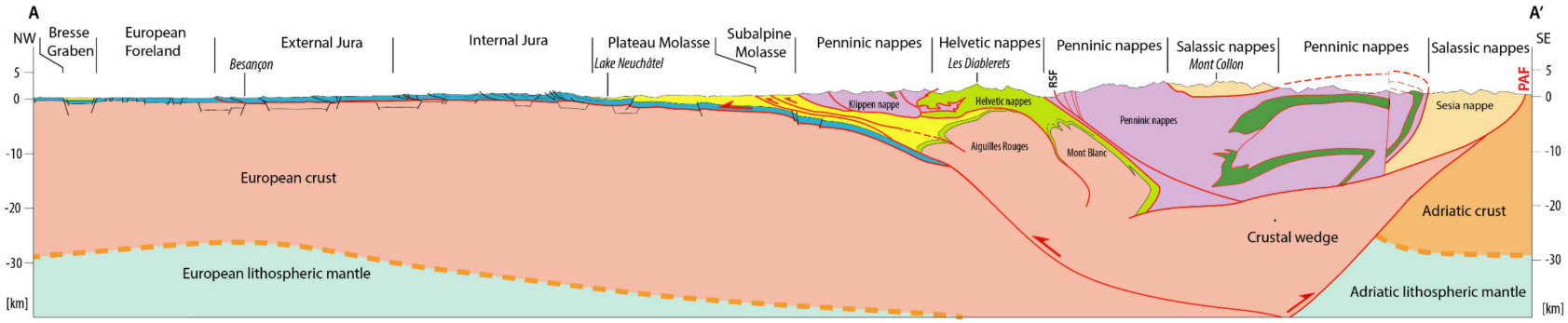

Figure 3. Cross section (SE-NW) through the Alps from the Po Basin to the Bresse graben (see Figure 2 for the section line). PAF: Peri-Adriatic fault system.

2. Previous Work

Central Europe was the site of widespread Triassic rifting followed by regional Triassic–Cretaceous marine sedimentation and complex accretion of the Iberian, Carnian and Apulian terranes [48,49]. Inversion of Permo-Mesozoic basement faults has been recognized in the Alps and the Alp foreland by Kley and Voight [44] as having been active in northern Europe in the Cretaceous. The Alps formed in the mid Cretaceous (ca. 100 Ma) and progressed from the Austroalpine in the Eastern Alps (as part of the Adriatic Plate) towards the west and north; the Central Swiss Alps were tectonized from the Paleocene through the Miocene. The inversion structures in northern Europe are the result of SSW-NNE shortening that ended by the Maastrichtian (72 Ma), a result that is in contrast to the Alpine–Carpathian orogen model proposed by Zeigler et al. ([50] and references therein). Opening of the Atlantic Ocean (58 Ma) coincided with the progradation of the Alpine orogen into the Central Swiss Alps and major northwest-directed nappe imbrication [51]. The Alps deformation, as recorded by offset synorogenic flysch deposits, apatite and zircon uplift ages and radiometric dates on metamorphic minerals, reveals a progression of orogenesis from the high-grade internal nappes in the northwest to the Jura Mountain folds and foreland that youngs toward the craton (NW; [23,26,52–57]). Palinspastic restorations indicate the Alps have been shortened ~60%, including folds, in the foreland (Figures 1–3), with significant transport-normal displacement on the Simplon–Rhone [58] and Insubric strike-slip systems [29,59,60], and were originally ~300–350 km wide. Alpine convergence also initiated a variety of Eocene extensional features in the foreland known as the European Cenozoic Rift System (ECRIS; [45,61–63]), which are unusual grabens not predicted by models of orogenic convergence where extensional features are observed within the high-grade internal portions of orogenic belts [64–67]. Evidence of extensional deformation in the Alpine nappes is poor, and the Proterozoic Keweenaw Rift–Grenville orogen provides one analog with foreland extension and rifting during a collisional orogen ([17] and references therein).

We provide a compilation of new (Irish coast, Alp foreland, Tauern window) and old (Jura, Molasse Basin, Helvetic and Penninic nappes) calcite twinning strain data across the Alps and the foreland to the northwest. Calcite, of course, is not the only means to record deformation: Siddans [68] reports a R_f/ϕ study of reduction spots in Permian mudstones from the basal Helvetic nappes along the Glarus thrust, where oblate ellipsoids (3:1.5:1 aspect ratios) have long axes oriented parallel to thrust transport and 20–30° to the thrust plane. This is a similar result to belemnite strain data in the Helvetic nappes reported by Ramsay [69] and Ramsay and Huber [70] and a fold-strain study by Pfiffner [71]. Studies of solution mass transfer (pressure solution) along the Glarus thrust reveal a volume loss of 36% of the hanging wall sediments [54,72]. Each of these strain results complements the twinning strain observations of Groshong et al. [73], namely the dominance of layer-normal shortening (LNS), in the Helvetic nappes, but they also reveal the value of using numerous techniques to measure strain [strain partitioning; [74]. Calcite and quartz tectonites have been studied in the Tauern window and the Penninic nappes [43,75,76] where calcitic pseudotachylite is found [75]. In the Alpine foreland, Lacombe et al. [7] first used a calcite twin paleostress (not strain) method to propose a complex tectonic history adjacent to the Jura Mountains, an approach similar to proxy structural methods (e.g., FAULTKIN, see [31,44,46,77–80]) and Ring and Gerdes ([45]; with U-Pb calcite ages) to interpret ~84 Ma of tectonic history in the European plate as Iberia accreted, the Atlantic Ocean opened, the Alps developed, and the ECRIS rift system evolved [81,82].

3. Methods

3.1. Calcite Twin Analysis

The calcite strain-gage technique (CSGT) of Groshong [83] uses intracrystalline twinning of rock-forming calcite grains to derive a three-dimensional orientation of the stress and strain ellipsoids during twinning. Although the result is a strain tensor, a similar orientation of the stress tensor is calculated in the case of coaxial deformation [84,85] he

CSGT has been used to constrain three-dimensional stress and strain tensor directions in calcite veins [6,16,86], limestone [6,39,87–96], marble [97], amygdaloidal basalt [47,98,99] calcite ocelli in lamprophyres [100] and fault gouge where calcite is dated with U–Pb methods [101–103]. Lacombe et al. [104]; this volume have reviewed the history and methods of calcite twin analysis.

Under temperatures of ca. 200 °C, intracrystalline deformation of calcite results in the formation of e-twins. The formation of calcite e-twins requires a shear stress exceeding ca. 10 MPa [105–108]. Calcite offers three glide systems for e-twinning. From U-stage measurements of width, frequency and orientation of twins, along with the crystallographic orientation of the host crystals, a strain tensor can be calculated using a least-squares technique [83]. To remove "noise" from the dataset, a refinement of the calculated strain tensor can be achieved by stripping 20% of the twins with the highest deviations [42]. This procedure has been used if the number of measured grains was large (n > 20). In cases where the data appear to be inhomogeneous, the separation of incompatible twins ("NEV" = negative expected values) from compatible twins ("PEV" = positive expected values) of the initial dataset allows for separate calculations of two or more least-squares deviatoric strain tensors. Thus, the CSGT can be used to obtain information on superimposed deformations [83,109] and differential stress magnitudes [110]. The validity of this stripping procedure was demonstrated in experimental tests where the reliability depends on the overall complexity of deformation and the number of grains with twins [109,111]. The stripping procedure was used in cases of high proportions of NEVs and many measured grains. An experimental re-evaluation of the CSGT has shown that measurements of about 50 grains on one thin section or 25 grains on two mutually perpendicular thin sections yield the best results [42,112,113] The chance to extract the records of more than two deformations from one dataset is limited when dealing with natural rocks [106]. Individual analyses of veins, matrix, nodules, etc., allow the acquisition of several strain tensors without applying statistical data stripping. Research on the complexity of rotational strains in fault zones is limited to the efforts of Gray et al. [114] and Craddock et al. [115], although the technique is more robust now that calcite can be dated using U-Pb methods [101]. Application of the CSGT requires the following assumptions to be valid: (1) low temperatures (dominance of Type I and Type II twins), (2) random c-axis orientations of calcite, (3) homogenous strain, (4) coaxial deformation, (5) volume constancy, (6) low-porosity materials and (7) low bulk strain (<15%). If these conditions are not fully met, calculated strain tensor datasets could be biased, modified or random. Strain tensors were calculated from calcite e-twin datasets using the software package of Evans and Groshong [112]. Fabric interpretations are based on the orientation of the shortening axis (e1), which usually plots near the contoured maxima of the Turner [84] compression axes, and if e1 is ~20° from the sample bedding great circle, layer-parallel shortening (LPS) is a valid fabric interpretation. Layer-normal shortening (LNS) is the fabric where e1 is at a high angle (>45°) to the bedding great circle; vein-normal (VNS) or vein-parallel (VPS) shortening are additional potential fabric interpretations (Table 2).

3.2. Calcite U-Pb Geochronology with LA-ICPMS-MC

Samples from Northern Ireland were examined under plane, polarized and cathodoluminescence (CL) microscopy to identify distinct precipitation phases yielding ages for veins PUE-17, 21, 23 and 26 (Table 1). U-Pb analyses of calcite were conducted at the University of California, Santa Barbara, following the protocol of Nuriel et al. [101], and are found in Appendix B.

4. Results

The opening of the Atlantic Ocean between Europe and Greenland (58 Ma; magnetochron 24) preceded the collision of Apulia into southern Europe that formed the Alps ~30 Ma, so our results are presented from oldest to youngest (Figure 1, Tables 1 and 2). Alpine geology is presented in Figures 2 and 3 (cross section). Field photos can be found

in Figures 4–6. Stereographic plots of twinning strain data can be found in Figure 4 (N. Ireland), Figures 7 and 8 (Alps and foreland), in Figures 9 and 10 (regional plots) and in Figure 11 (anomalous results). These results are compared with additional strain studies from the Alps (Table 2, see Appendix A for field locations).

Table 1. Summary Calcite Twinning Strain Data.

Location	Age	Samples	LS/Vein	Avg. NEV (%)	Avg.—e1 (%)	Avg. e1 (Tr and Plunge)	Avg. ds (Bars)	LNS/LPS	References
Atlantic Margin (N. Ireland)	58 Ma	16 (n = 454)	0/16	8	−3.41	50°, 1°	−387	0/16	This Study; U-Pb ages (Figure 4)
Alp Foreland	30 Ma	32 (n = 1648)	11/16	14	−4.98	310°, 5°	−343	4/28	This Study (Figure 5)
Jura Mountains	30 Ma	10 (n = 612)	10/0	26	−0.32	(See Figure 7)	No Data	0/28	[36]
Molasse Basin	30 Ma	26 (n = 1292)	26/0	21	−0.6	(See Figure 7)	No Data	1/25	[36,38]
Pre-Alps	30 Ma	39 (n = 2081)	26/13	30	−4.88	(See Figure 7)	No Data	20/19	[39]
Helvetic Nappes	30 Ma	17 (n = 112)	13/4	16	−3.66	(See Figure 7)	−372	10/7	[45,73]
Helvetic–Penninic Nappes	30 Ma	29 (n = 1450)	29/0	26	−6.6	(See Figure 7)	No Data	13/16	[40]
Austroalpine Nappes (Tauren)	30 Ma	4 (n = 1000)	Calcsilicate	26	−3.84	Vertical	−338	4/0	This Study (Figures 6 and 8)
Iceland	Active	19 (n = 430)	0/19	15	−6.02	Ridge-normal	−480	3/19	[47]
Gubbio Fault, Italy	Active	17 (n = 840)	0/17	4	−4.23	340°, 5°	−372	0/17	[115]
TOTALS		209 (n = 9919)	119/90						

Key: LPS is layer-parallel shortening; LNS is layer-normal shortening.

Table 2. Calcite strain data.

Sample	Section ID	Location	Rock Type	Bedding	Vein	Grains (n =)	e1	e2	e3	e1(%)	NEV (%)	Twins/mm	Ds (Bars)	Fabric (Bedding)	Fabric (Vein)	Orogenic Distance
Atlantic Margin (N. Ireland)																
24 (North)	PUE22	Port Rush, Ireland	Vein in Basalt	Horizontal	N-S, 90°	12	58°, 0°	328°, 2°	174°, 87°	−6.3	8	360	385.1277	LPS	VNS	1250 km
24	PUE23	Port Rush, Ireland	Vein in Basalt	Horizontal	N-S, 90°	22	26°, 2°	296°, 4°	132°, 86°	−3.4	18	456	402.683	LPS	VNS	1250
24	PUE24	Port Rush, Ireland	Vein in Basalt	Horizontal												
24	PUE25	Port Rush, Ireland	Vein in Basalt	Horizontal	N-S, 90°	24	186°, 3°	276°, 3°	48°, 85°	−1.9	8	446	401.0363	LPS	VPS	1250
24	PUE26	Port Rush, Ireland	Vein in Basalt	Horizontal	N-S, 90°	24	56°, 4°	146°, 2°	261°, 85°	−3.4	4	389	390.8814	LPS	VNS	1250
24	22, 23, 25	Port Rush, Ireland	Vein in Basalt	Horizontal	N-S, 90°	58	0°, 0°	270°, 1°	155°, 89°	−2.7	2	432	398.6677	LPS	VPS	1250
24	22, 26	Port Rush, Ireland	Vein in Basalt	Horizontal	N-S, 90°	36	9°, 1°	279°, 2°	140°, 87°	−2.5	11	416	395.865	LPS	VPS	1250
25	PUE17	Ballintoy Harbor, Ireland	LS/Vein	87°, 31° N	N-S, 90°	26	257°, 1°	347°, 1°	104°, 88°	−3.6	8	421	396.7522	LPS	VNS	1250
25	PUE18	Ballintoy Harbor, Ireland	LS/Vein	87°, 31° N	E-W, 90°	20	209°, 1°	300°, 2°	88°, 86°	−4.7	20	295	370.3396	LPS	VNS	1250
25	PUE19	Ballintoy Harbor, Ireland	Vein in LS	87°, 31° N	N-S, 90°	25	211°, 1°	302°, 1°	68°, 88°	−6.2	0	278	365.9317	LPS	VNS	1250
25	PUE20	Ballintoy Harbor, Ireland	Vein in Basalt	Horizontal	E-W, 90°	25	40°, 2°	311°, 1°	181°, 88°	−4.2	12	548	416.3315	LPS	VNS	1250
25	PUE21	Ballintoy Harbor, Ireland	Vein in Basalt	Horizontal	E-W, 90°	22	12°, 1°	101°, 3°	273°, 86°	−4.4	0	469	404.7706	LPS	VNS	1250
25	20,21	Ballintoy Harbor, Ireland	Vein in Basalt	Horizontal	E-W, 90°	47	28°, 2°	301°, 3°	143°, 86°	−4.3	6	508	410.7027	LPS	VNS	1250
23	PUE13	Moneymore, Ireland	LS/Vein	Horizontal	0°, 90°	23	250°, 19°	159°, 1°	65°, 70°	−1.9	11	407	394.2406	LPS	VNS	1200
23	PUE14	Moneymore, Ireland	LS/Vein	Horizontal												
23	PUE15	Moneymore, Ireland	LS/Vein	Horizontal	0°, 90°	20	252°, 4°	162°, 1°	67°, 85°	−1.6	20	237	354.082	LPS	VPS	1200
23	PUE16	Moneymore, Ireland	LS/Vein	Horizontal	0°, 90°	25	266°, 1°	354°, 1°	152°, 88°	−1.8	4	261	361.2455	LPS	VNS	1200
23	15 & 16	Moneymore, Ireland	Veins	Horizontal	0°, 90°	45	218°, 1°	308°, 2°	85°, 87°	−1.7	0	252	358.6395	LPS	VNS	1200
						454				−3.4125	8.25		387.9561			
Alpine Foreland (NW)																
	PUE1	Hull, UK	LS/Vein	Horizontal		No twins										
22	OSE15	Gloucester, UK	LS	22°, 12° SE		12	22°, 8°	112°, 1°	206°, 81°	−2.3	25	312	374.5004	LPS		800
22	OSE16	Gloucester, UK	Vein in LS	22°, 12° SE	72°, 90°	18	340°, 23°	79°, 5°	175°, 65°	−8.5	11	385	390.1138	LPS	VNS	800
22	15 & 16	Gloucester, UK	LS/Vein	22°, 12° SE	72°, 90°	30	350°, 10°	266°, 1°	176°, 80°	−13.3	20	373	387.7622	LPS	VNS	800
21	OSE13	Bath, UK	LS	45°, 7° SE		No twins										
21	OSE14	Bath, UK	LS	45°, 7° SE		13	310°, 21	213°, 12°	95°, 65°	−4.3	23	162	325.8271	LPS		750
20	PUE11	Cheddar Gorge, UK	Vein	12°, 15° S	Horizontal	23	219°, 23°	128°, 1°	38°, 66°	−5.9	11	262	361.5295	LPS	VPS	715
20	PUE12	Cheddar Gorge, UK	LS	12°, 15° S	Horizontal	27	334°, 4°	64°, 1°	183°, 86°	−3.1	11	337	380.2247	LPS		715
20	PUE12	Cheddar Gorge, UK	Vein	12°, 15° S	61°, 48° S	26	158°, 1°	68°, 2°	261°, 88°	−1.9	3	357	384.5063	LPS	VNS	715
19	PUE10	Birdport, UK	LS	Horizontal		No twins										
18	PUE8	Lulworth Cove, UK	Vein	Horizontal	Horizontal	27	176°, 4°	84°, 1°	303°, 85°	−5.5	0	307	373.3007	LPS	VPS	680
18	PUE9	Lulworth Cove, UK	LS	90°, 23° N		No twins										
17	6&7 PEV	Corfe Castle, UK	Vein	Horizontal	110°, 82° S	39	120°, 76°	260°, 10°	352°, 8°	−1.9	0	164	326.7383	LNS	VNS	680
17	6&7 NEV	Corfe Castle, UK	Vein	Horizontal	110°, 82° S	23	210°, 75°	358°, 11°	90°, 7°	−4.8	100	125	306.5716	LPS	VNS	680
15	PUE2	W. Isle of Wight, UK	LS/Vein	Horizontal	Horizontal	20	153°, 19°	58°, 7°	318°, 55°	−8.5	15	213	346.1529	LPS	VPS	610
15	PUE3	W. Isle of Wight, UK	LS/Vein	Horizontal	Horizontal	9	143°, 6°	234°, 5°	1°, 81°	−7.9	0	250	358.0477	LPS	VPS	610
16	PUE2&3	W. Isle of Wight, UK	LS/Vein	Horizontal	Horizontal	29	153°, 11°	61°, 5°	315°, 71°	−9.4	31	220	348.5543	LPS	VPS	610
	PUE4	W. Isle of Wight, UK	LS/Vein	Horizontal		No twins										
	PUE5	E. Isle of Wight, UK	LS/Vein	Horizontal		No twins										
14	OSE17	Audreselles, France	Vein	Horizontal	341°, 90°	18	260°, 23°	95°, 65°	351°, 5°	−2.8	0	229	351.5319	LPS	VNS	510
14	OSE18	Audreselles, France	Vein	Horizontal	0°, 90°	18	132°, 2°	41°, 10°	238°, 79°	−2.8	16	245	356.5474	LPS	VNS	510
14	OSE19	Audreselles, France	Vein	Horizontal	0°, 90°	20	175°, 29°	79°, 12°	339°, 62°	−5.7	20	173	330.7059	LPS	VPS	510
14	18 &19	Audreselles, France	Veins	Horizontal	0°, 90°	54	145°, 18°	53°, 4°	310°, 70°	−6.2	31	208	344.3888	LPS	VNS	480
14	OSE19	Audreselles, France	LS	Horizontal		18	125°, 1°	28°, 3°	223°, 86°	−1.8	0	246	356.8499	LPS		480

Table 2. *Cont.*

Sample	Section ID	Location	Rock Type	Bedding	Vein	Grains (n =)	e1	e2	e3	e1(%)	NEV (%)	Twins/mm	Ds (Bars)	Fabric (Bedding)	Fabric (Vein)	Orogenic Distance
Alpine Foreland (NW)																
13	OSE20	Boulogne, France	Vein	Horizontal	0°, 90°	23	170°, 11°	269°, 1°	3°, 78°	−1.8	0	259	360.6743	LPS	VPS	480
13	OSE21	Boulogne, France	Vein	Horizontal	0°, 90°	20	201°, 5°	291°, 1°	32°, 84°	−5.9	10	172	330.2754	LPS	VPS	480
13	20&21	Boulogne, France	Veins	Horizontal	0°, 90°	43	193°, 6°	103°, 1	1°, 82°	−5.7	2	224	349.8924	LPS	VPS	480
	OSE22	Paris, France	LS	Horizontal		No twins										
	OSE23	Paris, France	LS	Horizontal		No twins										
12	OSE12	Pottenstein, Germany	LS	Horizontal		No twins										
11	OSE11PEV	Grafenberg, Germany	Vein in LS	Horizontal	343°, 90°	31	345°, 9°	77°, 14°	223°, 73°	−1.3	0	194	339.2141	LPS	VPS	230
11	OSE11NEV	Grafenberg, Germany	Vein in LS	Horizontal	343°, 90°	19	358°, 62°	99°, 5°	192°, 27°	−9.6	100	333	379.338	LNS	VNS	230
5	OSE5	Saints-Geosmes, France	LS	Horizontal		24	181°, 1°	271°, 7°	81°, 82°	−1.1	0	210	345.0995	LPS		160
6	OSE6&7N	Chatenois, France	LS	Horizontal		21	11°, 76°	181°, 12°	272°, 2°	−2.6	100	164	326.7383	LNS		170
7	OSE6&7P	Graux, France	LS	Horizontal		26	172°, 7°	262°, 4°	22°, 81°	−13.4	30	204	342.9468	LPS		140
8	OSE8	Nancy, France	LS	Horizontal		18	132°, 5°	40°, 10°	250°, 78°	−3.1	5	110	297.0781	LPS		130
9	OSE9	Wiesensteig, Germany	LS	Horizontal		No twins										100
10	OSE10	Solnhofen, Germany	LS	Horizontal		No twins										145
4	OSE3 & 4N	N. Champlitte, France	LS	Horizontal		19	167°, 63°	16°, 23°	281°, 11°	−3.14	100	100	290	LNS		140
2	OSE3 & 4P	Champlitte, France	LS	Horizontal		25	330°, 30°	48°, 24°	166°, 46°	−2.94	0	117	301.6598	LPS		100
2	OSE1 & 2N	Taxenne, France	LS	Horizontal		27	136, 13°	226°, 1°	351°, 56°	−1.56	100	131	310.0534	LPS		30
1(South)	OSE1 & 2P	Besancon, France	LS	Horizontal		20	348°, 3°	252°, 1°	147°, 86°	−2.54	0	164	326.7383	LPS		5
						1648				−4.88	14.25		345.276			
Jura Mtns. [36]																
5		Mamirolle, France	Jurassic LS			62	20°, 17°	177°, 71°	288°, 7°	−0.5	27			LPS		
6		Mamirolle, France	Jurassic LS			42	61°, 40°	173°, 23°	284°, 41°	−1.9	33			LPS		
11		Mamirolle, France	Jurassic LS			63	345°, 13°	248°, 27°	98°, 58°	−0.8	30			LPS		
19		Mamirolle, France	Jurassic LS			57	8°, 3°	270°, 27°	137°, 86°	−0.6	10			LPS		
21		Mamirolle, France	Jurassic LS			60	190°, 37°	22°, 53°	284°, 6°	−3.4	15			LPS		
5		Dole, France	Jurassic			43	143°, 59	245°, 6°	339°, 29°	1.1	18			LPS		
8b		Dole, France	Jurassic			73	344°, 14°	252°, 1°	162°, 16°	1.7	31			LPS		
8c		Dole, France	Jurassic			63	192°, 13°	292°, 35°	85°, 51°	0.7	31			LPS		
9		Dole, France	Jurassic			71	199°, 20°	316°, 51°	96°, 31°	5.1	42			LPS		
10		Dole, France	Jurassic			78	191°, 47	53°, 33°	308°, 22°	1.8	26			LPS		
						612				0.32	26.3					
Val-de-Ruz area ([36], Molasse Basin)																
1		Val-de-Ruz, Switzerland	Valanginian	80, 12S		30	166°, 13°	262°, 24°	45°, 31°	1.2	35			LPS		
2		Val-de-Ruz, Switzerland	Malm	52, 47S		64	5°, 44°	110°, 16°	215°, 42°	2.8	28			LNS		
3		Val-de-Ruz, Switzerland	Malm	92, 8S		50	157°, 16°	248°, 4°	32°, 61°	2.1	22			LPS		
4		Val-de-Ruz, Switzerland	Dogger	73, 82S		57	177°, 64°	4°, 26°	312°, 9°	2.0	17			LPS		
5		Val-de-Ruz, Switzerland	Malm	71, 28S		45	207°, 18°	60°, 70°	129°, 12°	1.1	20			LPS		
6		Val-de-Ruz, Switzerland	Malm	Horizontal		43	137°, 5°	47°, 3°	302°, 15°	0.9	30			LPS		
7		Val-de-Ruz, Switzerland	Valanginian	83, 12S		44	311°, 40°	74°, 33°	156°, 6°	2.6	34			LPS		

Table 2. *Cont.*

Sample	Section ID	Location	Rock Type	Bedding	Vein	Grains (n =)	e1	e2	e3	e1(%)	NEV (%)	Twins/mm	Ds (Bars)	Fabric (Bedding)	Fabric (Vein)	Orogenic Distance
Molasse Basin [38]																
dh4		Neuchatel, Switzerland	Miocene	Horizontal		51	87°, 15°	353°, 14°	222°, 69°	0.15	20			LPS		
dh5		Neuchatel, Switzerland	Miocene	Horizontal		53	145°, 4°	235°, 1°	341°, 86°	0.14	23			LPS		
dh8		Neuchatel, Switzerland	Miocene	Horizontal		51	183°, 25°	321°, 58°	84°, 19°	0.16	27			LPS		
dh12		Neuchatel, Switzerland	Miocene	Horizontal		51	150°, 49°	241°, 1°	332°, 41°	0.12	20		−128	LPS		
dh15		Neuchatel, Switzerland	Miocene	Horizontal		51	18°, 8°	286°, 9°	149°, 78°	0.14	16		−137	LPS		
dh17		Neuchatel, Switzerland	Miocene	Horizontal		51	74°, 1°	344°, 27°	165°, 63°	0.09	29			LPS		
dh2l		Neuchatel, Switzerland	Miocene	Horizontal		51	341°, 15°	84°, 41°	235°, 45°	0.15	12		−191	LPS		
dh2		Neuchatel, Switzerland	Miocene	Horizontal		51	153°, 3°	249°, 64°	62°, 26°	0.13	31			LPS		
dh22		Neuchatel, Switzerland	Miocene	Horizontal		51	164°, 20°	41°, 56°	264°, 26°	0.14	18			LPS		
dh24		Neuchatel, Switzerland	Miocene	Horizontal		51	165°, 19°	257°, 6°	5°, 70°	0.11	22		−161	LPS		
dh26		Neuchatel, Switzerland	Miocene	Horizontal		51	190°, 34°	89°, 13°	344°, 48°	0.09	29			LPS		
dh28		Neuchatel, Switzerland	Miocene	Horizontal		51	145°, 4°	237°, 24°	47°, 66°	0.14	2			LPS		
dh3l		Neuchatel, Switzerland	Miocene	Horizontal		51	145°, 17°	343°, 72°	237°, 5°	0.07	25			LPS		
dh32		Neuchatel, Switzerland	Miocene	Horizontal		51	144°, 8°	54°, 4°	297°, 81°	0.24	10			LPS		
dh37		Neuchatel, Switzerland	Miocene	Horizontal		51	116°, 6°	19°, 50°	211°, 40°	0.14	12			LPS		
dh39		Neuchatel, Switzerland	Miocene	Horizontal		51	108°, 14°	18°, 2°	281°, 76°	0.11	25			LPS		
dh40		Neuchatel, Switzerland	Miocene	Horizontal		39	260°, 12°	352°, 7°	109°, 76°	0.11	21			LPS		
dh4l		Neuchatel, Switzerland	Miocene	Horizontal		51	40°, 2°	309°, 4°	153°, 86°	0.11	12			LPS		
dh42		Neuchatel, Switzerland	Miocene	Horizontal		51	232°, 24°	141°, 3°	44°, 86°	0.1	10		−132	LPS		
						1292				0.6	21.15385					
Pre-Alps [39]																
41		Pre-Alp Medianes nappe	Malm	38°, 47° N		53	155°, 78°	322°, 41°	41°, 8°	−5.12	34			LNS		
47		Pre-Alp Medianes nappe	Malm	21°, 46° N		51	312°, 33°	71°, 80°	212°, 22°	−2.71	43			LPS		
81		Pre-Alp Medianes nappe	Malm, vein	300°, 70° S	?	52	120°, 23°	45°, 3°	302°, 62°	−2.81	29			LPS	?	
82		Pre-Alp Medianes nappe	Dogger, vein	302°, 60° S	?	53	161°, 12°	261°, 5°	348°, 81°	−2.5	32			LNS	?	
84		Pre-Alp Medianes nappe	Flysch	105°, 88° N		54	205°, 31°	22°, 47°	111°, 3°	−3.73	30			LNS		
85V		Pre-Alp Medianes nappe	Flysch, vein		?	58				−3.9	31			LPS	?	
85		Pre-Alp Medianes nappe	Flysch	71°, 45°N		52	352°, 41°	142°, 28°	251°, 4°	−3.87	44			LPS		
86		Pre-Alp Medianes nappe	Neocom	Horizontal		55	201°, 11°	311°, 41°	92°, 46°	−2.88	18			LPS		
87		Pre-Alp Medianes nappe	Neocom	88°, 47° S		55	222°, 18°	20°, 82° S	142°, 3°	−1.86	46			LPS		
88		Pre-Alp Medianes nappe	Neocom, vein	45°, 22°N	?	56	118°, 72°	2°, 3°	122°, 81°	−7.68	20			LNS	?	
89		Pre-Alp Medianes nappe	Lias	65°, 85°N		59	120°, 82	1°, 1°	270°, 5°	−5.36	36			LPS		
90		Pre-Alp Medianes nappe	Malm, vein	300°, 45° S	?	73	240°, 38°	121°, 11°	12°, 41°	−2.81	33			LPS	?	
91		Pre-Alp Medianes nappe	Dogger, vein	100°, 70° S	?	52	112°, 22°	10°, 12°	255°, 42°	−3.99	25			LPS	?	
92		Pre-Alp Medianes nappe	Dogger, vein	100°, 70° S	?	57	181°, 88°	330°, 2°	64°, 1°	−1.95	19			LPS	?	
93		Pre-Alp Medianes nappe	Dogger	Horizontal		54	271°, 58°	92°, 11°	190°, 1°	−3.21	32			LNS		
98		Pre-Alp Medianes nappe	Dogger	52°, 88°N		51	51°, 35°	202°, 41°	305°, 12°	−4.23	29			LPS		
100		Pre-Alp Medianes nappe	Lias, vein	Horizontal	?	46	185°, 72°	88°, 4°	351°, 5°	−3.35	35			LNS	?	
102		Pre-Alp Medianes nappe	Dogger	81°, 70°N		53	168°, 5°	271°, 45°	72°, 5°	−4.91	11			LNS		
105		Pre-Alp Medianes nappe	Flysch	91°, 80°N		99	182°, 7°	351°, 79°	101°, 4°	−5.61	24			LNS		
105V		Pre-Alp Medianes nappe	Flysch, vein		?	51				−6.17	10			LPS	?	
53		Pre-Alp Medianes nappe	Vein	5°, 70°W	?	57	123°, 47°	227°, 44°	352°, 41°	−2.46	39			LNS	?	
94		Pre-Alp Medianes nappe	Lias	338°, 75°		50	331°, 51°	153°, 62°	247°, 5°	−6.26	28			LNS		

Table 2. *Cont.*

Sample	Section ID	Location	Rock Type	Bedding	Vein	Grains (n =)	e1	e2	e3	e1(%)	NEV (%)	Twins/mm	Ds (Bars)	Fabric (Bedding)	Fabric (Vein)	Orogenic Distance
Pre-Alps [39]																
64		Pre-Alp Rigid nappe	Malm	38°, 31° S		41	41°, 35°	242°, 31°	138°, 1°	−3.75	44			LNS		
72		Pre-Alp Rigid nappe	Trias	51°, 20° S		52	162°, 31°	270°, 1°	2°, 47°	−1.85	25			LPS		
73		Pre-Alp Rigid nappe	Trias, vein	44°, 21° S	?	51	122°, 20°	203°, 2°	303°, 62°	−2.72	33			LPS	?	
76		Pre-Alp Rigid nappe	Flysch, vein	21°, 62° S	?	57	242°, 18°	342°, 31°	106°, 58°	−2	32			LNS	?	
106		Pre-Alp Rigid nappe	Trias	Horizontal		50	135°, 6°	267°, 82°	44°, 2°	−5.48	34			LPS		
109		Pre-Alp Rigid nappe	Malm, vein	45°, 6° S	?	46	135°, 88°	272°, 2°	22°, 3°	−13.05	35			LNS	?	
110		Pre-Alp Rigid nappe	Malm	45°, 23° S		45	342°, 31°	182°, 41°	83°, 5°	−8.38	42			LPS		
129		Pre-Alp Rigid nappe	Dogger	2°, 47° E		47	273°, 14°	182°, 1°	88°, 42°	−9.7	21			LNS		
132		Pre-Alp Rigid nappe	Malm	18°, 41° E		48	233°, 51°	26°, 21°	131°, 3°	−9.05	23			LNS		
133		Pre-Alp Rigid nappe	Malm	21°, 12° E		48	282°, 62°	177°, 6°	83°, 12°	−9.48	13			LNS		
135		Pre-Alp Rigid nappe	Malm	Horizontal		48	186°, 9°	311°, 41°	82°, 22°	−7.33	38			LPS		
136		Pre-Alp Rigid nappe	Trias, vein	38°, 28° S	?	48	251°, 22°	347°, 12°	117°, 33°	−3.04	31			LNS	?	
137		Pre-Alp Rigid nappe	Trias	41°, 25° E		46	252°, 47°	87°, 30°	352°, 8°	−7.54	26			LNS		
78		Gurnigel nappe	Flysch			53				−2.17	26			LPS		
74		Gurnigel nappe	Breche nappe	Horizontal		54	136°, 2°	52°, 5°	302°, 83°	−3.2	35			LPS		
61		Gurnigel nappe	Flysch	51°, 46° S		50	350°, 43°	161°, 44°	258°, 2°	−7.05	35			LNS		
69		Gurnigel nappe	Flysch	12°, 41° E		56	183°, 41°	73°, 11°	322°, 26°	−7.14	27			LNS		
						2081				−4.8795	29.94872			LNS = 20/ LPS = 19		
Helvetic Nappes [73]																
80-21		Santis Thrust	K limestone				181°, 1°			−4.2	20			LNS		
80-23		Santis Thrust	K limestone				172°, 5°			−0.5	19			LPS		
80-24		Santis Thrust	K limestone				205°, 22°			−2.9	9			LNS		
80-25		Santis Thrust	K limestone				172°, 12°			−3.4	13			LPS		
80-15		Santis Thrust	K limestone				153°, 30°			−2	16			LPS		
80-14		Glarus Thrust	K limestone				342°, 82°			−1.1	12			LNS		
80-11		Murtschen Thrust	K limestone				0°, 82°			−5.7	8			LNS		
80-12		Murtschen Thrust	K limestone				340°, 81°			−5.7	25			LNS		
80-13		Murtschen Thrust	K limestone				276°, 84°			−8.9	17			LPS		
80-16		Glarus Footwall	K limestone				284°, 77°			−1.9	11			LPS		
80-17		Glarus Footwall	K limestone				78°,82°			−5.3	16			LPS		
80-19		Glarus Footwall	K limestone				330°, 45°			−3	18			LPS		
80-20		Glarus Footwall	K limestone				271°, 33°			−3	27			LNS		
										−3.6615	16.23077			LNS = 6/LPS = 7		
Helvetic Nappes (this study)																
BE-2416	BE-2416	Alpenrhein Graben	Vein (striated)	48° E, 42° S	6°, 82°W	22	348°, 5°	269°, 4°	153°, 88°	−6.3	9	276	365.395	LNS	VNS	0
H2	H2	Alpenrhein Graben	Vein (striated)	73° E, 33° S	63°, 79° E	36	171°, 3°	274°, 13°	47°, 78°	−1.63	11	179	333.238	LNS	VNS	0
H3	H3	Alpenrhein Graben	Vein (striated)	69° E, 24° S	349°, 86°W	18	157°, 4°	27°, 7°	246°, 86°	−6.43	22	366	386.355	LNS	VNS	0
H4	H4	Alpenrhein Graben	Vein (striated)	87° E, 16° S	7°, 55° E	36	168°, 8°	281°, 27°	96°, 41°	−3.34	8	483	406.955	LNS	VPS	0
						n = 112				−4.43	12.5		−372.25	LNS = 4/LPS = 0		
Helvetic–Penninic Nappes [40]																
J20		Dolden–Wildhorn nappes	Valanginian	0, 0		50	352°, 16°	234°, 16°	90°, 26°	5.0	25			No plot; LPS		
J30V		Dolden–Wildhorn nappes	Valanginian	180, 30		50	298°, 8°	40°, 56°	203°, 33°	6.0	10			No plot; LPS		
J30M		Dolden–Wildhorn nappes	Valanginian	180, 30		50	195°, 24°	99°, 14°	340°, 62°	5.0	25			No plot; LPS		
J31V		Dolden–Wildhorn nappes	Valanginian	180, 30		50	313°, 37°	186°, 38°	69°, 29°	3.0	29			No plot; LPS		

Table 2. *Cont.*

Sample	Section ID	Location	Rock Type	Bedding	Vein	Grains (n =)	e1	e2	e3	e1(%)	NEV (%)	Twins/mm	Ds (Bars)	Fabric (Bedding)	Fabric (Vein)	Orogenic Distance
Helvetic–Penninic Nappes [40]																
G1M		Dolden–Wildhorn nappes	Valanginian	240, 22		50	303°, 45°	151°, 42°	47°, 14°	6.0	18			LPS		
G1V		Dolden–Wildhorn nappes	Valanginian	240, 22		50	271°, 39°	132°, 43°	20°, 22°	5.0	18			LPS		
Ge1		Dolden–Wildhorn nappes	Malm	290, 20		50	64°, 41°	320°, 16°	213°, 45°	6.0	30			LNS		
A3		Dolden–Wildhorn nappes	dogger	308, 46		50	8°, 16°	115°, 45°	265°, 40°	3.0	42			LPS		
L13V		Dolden–Wildhorn nappes	Malm	190, 40		50	16°, 25°	240°, 56°	116°, 20°	7.0	43			LNS		
L13M		Dolden–Wildhorn nappes	Malm	190, 40		50	118°, 40°	14°, 17°	265°, 45°	9.0	30			LPS		
W17		Dolden–Wildhorn nappes	Malm	234, 14		50	126°, 13°	321°, 76°	217°, 3°	3.0	17			LPS		
W50		Dolden–Wildhorn nappes	Malm	240, 18		50	273°, 6°	19°, 70°	181°, 20°	5.0	32			LPS		
W68		Dolden–Wildhorn nappes	Malm	310, 56		50	265°, 67°	134°, 16°	39°, 17°	9.0	32			LPS		
W72		Dolden–Wildhorn nappes	Barremian	225, 50		50	276°, 77°	82°, 13°	172°, 3°	4.0	35			LPS		
W77		Dolden–Wildhorn nappes	Barremian	110, 75		50	359°, 41°	169°, 49°	265°, 5°	2.0	22			LNS		
W90		Dolden–Wildhorn nappes	Barremian	310, 56		50	354°, 48°	258°, 6°	163°, 41°	15.0	16			LPS		
M129		Dolden–Wildhorn nappes	Valanginan	350, 9		50	274°, 70°	156°, 9°	63°, 17°	18.0	20			LNS		
M130		Dolden–Wildhorn nappes	Valanginan	300, 16		50	134°, 58°	30°, 8°	295°, 30°	2.0	29			LNS		
M133		Dolden–Wildhorn nappes	Eocene	290, 40		50	312°, 32°	143°, 58°	45°, 58°	2.0	30			LPS		
M156		Dolden–Wildhorn nappes	Eocene	316, 44		50	325°, 37°	186°, 45°	73°, 22°	6.0	8			LPS		
M170		Dolden–Wildhorn nappes	Malm	328, 35		50	106°, 46°	235°, 31°	344°, 27°	8.0	20			LNS		
M174		Dolden–Wildhorn nappes	Barremian	28, 50		50	182°, 52°	334°, 35°	73°, 14°	6.0	29			LNS		
M175		Dolden–Wildhorn nappes	Barremian	30, 30		50	201°, 49°	0°, 40°	99°, 11°	4.0	30			LNS		
M186		Dolden–Wildhorn nappes	Barremian	0,0		50	142°, 40°	33°, 21°	282°, 43°	6.0	17			LPS		
M191		Dolden–Wildhorn nappes	Valanginan	286, 25		50	354°, 51°	145°, 35°	245°, 15°	14.0	25			LNS		
M199		Dolden–Wildhorn nappes	Valanginian	296, 11		50	37°, 78°	269°, 10°	177°, 7°	9.0	27			LNS		
M220		Dolden–Wildhorn nappes	Dogger	304, 40		50	152°, 68°	56°, 3°	325°, 21°	9.0	28			LNS		
M245		Dolden–Wildhorn nappes	Eocene	160, 40		50	136°, 71°	324°, 19°	234°, 3°	5.0	29			LNS		
M356		Dolden–Wildhorn nappes	Dogger	0,0		50	190°, 71°	299°, 3°	30°, 11°	8.0	35			LNS		
						1450				6.6	25.89655			LNS = 13/ LPS = 16		
Tauren Window, Austria																
17,651/17,653	NEV	Tauren Window, Austria	Calcsilicate	N-S Sheath fold		78	1°, 72°	192°, 1°	263°, 8°	−2.21	100	140	314.988	LNS		
289a6/298a7	NEV	Tauren Window, Austria	Calcsilicate	N-S Sheath fold		62	38°, 83°	171°, 12°	84°, 2°	−1.74	100	108	295.715	LNS		
72,664/74,664	NEV	Tauren Window, Austria	Calcsilicate	N-S Sheath fold		73	183°, 87°	145°,6°	86°, 5°	−1.83	100	221	348.891	LNS		
801a1/801a2	NEV	Tauren Window, Austria	Calcsilicate	N-S Sheath fold		66	231°, 69°	133°,6°	88°, 4°	−2.57	100	240	355.016	LNS		
						279				−2.08			−328			
	Avg. of all Tauren samples					1000				−3.612	29.1		−337.351			

Key: E1 = maximum shortening axis; E2 = intermediate axis; E3 = extension axis. LPS = layer-parallel shortening; LNS = layer-normal shortening; VPS = vein-parallel shortening; VNS = vein-normal shortening; $\Delta\sigma = -51 + \log 171$ (#twins/mm).

4.1. Irish Tertiary Province

In central Northern Ireland, near Moneymore, a number of quarries expose interlayered Cretaceous chalks and limestones and Tertiary (70–42 Ma) basalt sills, flows and crosscutting dikes. Calcite veins are present throughout, and normal faults with calcite fillings (various strikes, steep northerly dips and striated calcite steps: top-down-to-the-north) are common in the limestones. Four calcite veins have U-Pb ages between 70–42 Ma, similar in age to calcite vein fillings along the Atlantic margin in the Faroe Islands (Figure 4; [116]). Along the northern coast, between Port Rush and Ballycastle, similar basalt–limestone contacts are exposed, but more pervasive structures are present; at Ballintoy Harbor, orthogonal (N-S, 90° and E-W, 90°) faults are present, and both preserve sinistral offsets (Figure 4). Calcite veins are also thicker and more pervasive here, and a normal fault hanging wall anticline is present with calcite fillings associated with the normal fault offset. All thirteen samples (n = 202 grains) from 3 different locations preserve the same calcite strain fabric: SE-NW sub-horizontal shortening and vertical extension that is parallel to the Atlantic margin opened by SE-NW extension. The calcite preserves modest strains (average shortening −3.1%), with no suggestion of any strain overprint (average NEVs 8%) and a modest differential stress associated with the opening of the Atlantic Ocean (average −387 bars, Tables 1 and 2). The highest strain magnitude (−6.3%) is at the coast, and the lowest (−1.7%) is inland near Moneymore, a distance of ~50 km. Fabric interpretation is based on the orientation of the maximum shortening axis (e_1) relative to bedding, and all 16 samples preserve a layer-parallel shortening (LPS) strain where e_1 is +/− 20° from bedding. Conversely, as all the samples are veins or fault fillings, the orientation of e_1 relative to the vein-filling provides an additional fabric insight: 4 VPS (vein-parallel shortening) and 12 VNS (vein-normal shortening) fabrics are preserved. Interestingly, samples 7, 8, and 11–14, which have sinistral and normal kinematics, respectively, all preserve the same NE-SW margin-parallel, sub-horizontal shortening.

4.2. Internal Alps

Alpine exhumation has exposed the Austroalpine Variscan continental crust to the south of the Tauern Window, the Austrian Alps (Figures 1–3). Variscan ductile deformational is characterized by garnet–staurolite and kyanite-bearing biotite–plagioclase paragneisses that are mainly the result of non-coaxial progressive shearing D_1-D_2 with isoclinal folds and a subsequent folding (D_3) around the lineation L_2 [117]. Both deformation events are older than mica cooling age of 300 Ma [118,119]. The paragneisses include dm-scaled sheath-like folded calcsilicate-gneiss bodies, which are elongated parallel to lineation L2 (Figure 6). Quartz c-axis fabrics signal deformation partitioning with non-coaxial shearing parallel to lineation and elongation axis along the margin of the body and coaxial deformation (flattening and constriction) in the center. Porphyroblastic garnets and local C-S offsets in the paragneiss host rock indicate the same sense of shear. Calcite is intergrown with all the main metamorphic mineral phases, including as tail growths on garnet porphyroblasts, and mechanical twins are thus interpreted as primary recorders of the Variscan stress–strain history. Twelve thin sections were analyzed (n = 769), and all had a high percentage of the secondary negative expected values (30–35%), such that two strain events were separated (PEV and NEV; Erickson et al. 2006; Tables 1 and 2). The two events are shortening parallel to the axis of the sheath fold (~N-S; PEV) and vertical shortening (NEV), presumably related to Alpine exhumation and nappe stacking. The NEV twinning strain overprint records extension parallel to the short axes of the bodies, corroborating the quartz fabric data. The average shortening strain was −4.62%, and the average differential stress associated with twinning was −339 bars.

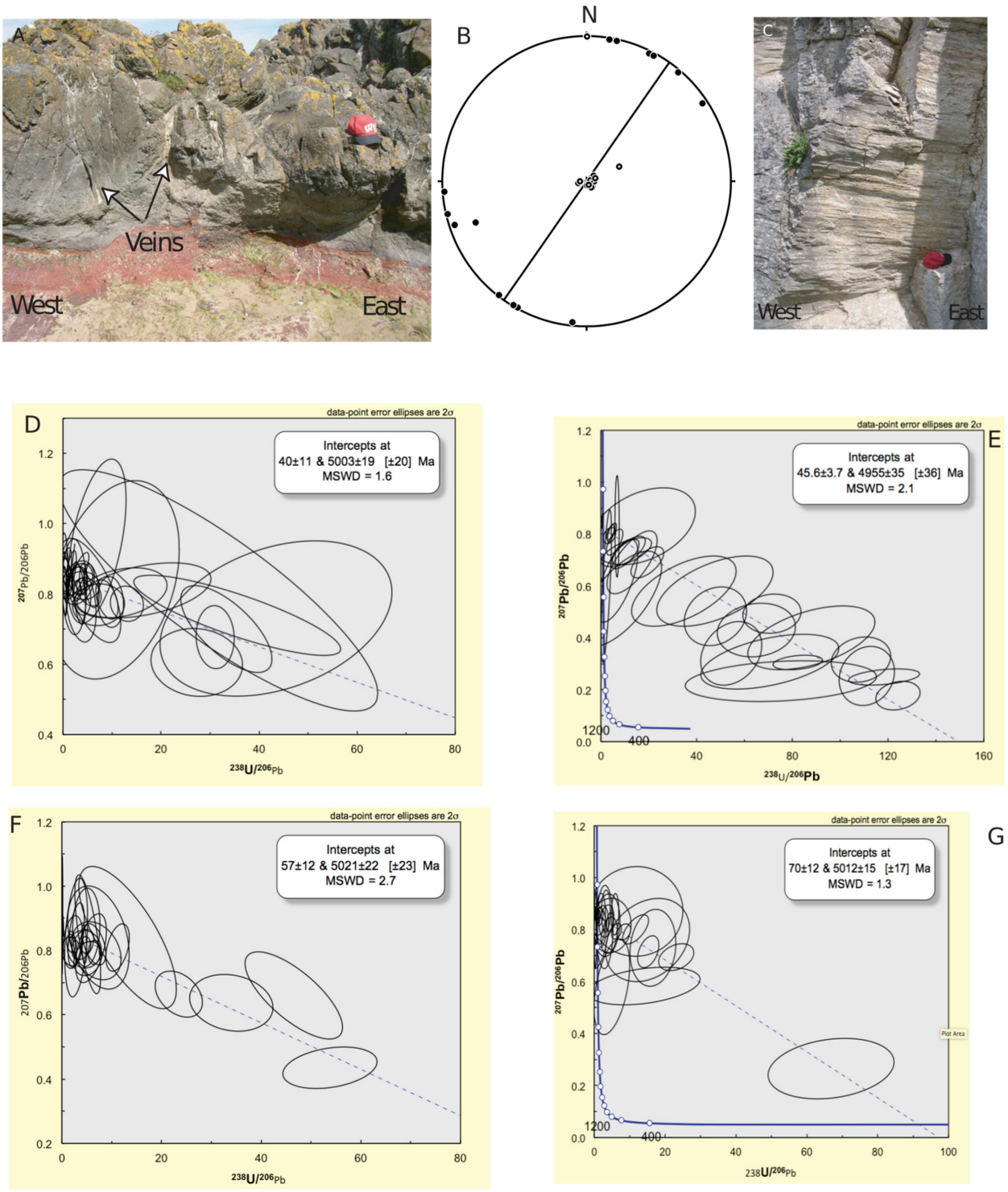

Figure 4. Tertiary basalts (**A**) from the northern coast of Ireland with calcite veins and horizontal striations on Cretaceous limestones (**C**). Calcite twinning strains for all data (Tables 1 and 2, Appendix A; solid circles = shortening axes, open circles = extension axes in (**B**). Tera–Wasserburg plots of U-Pb ages on vein calcite ((**D**–**G**); Appendix B).

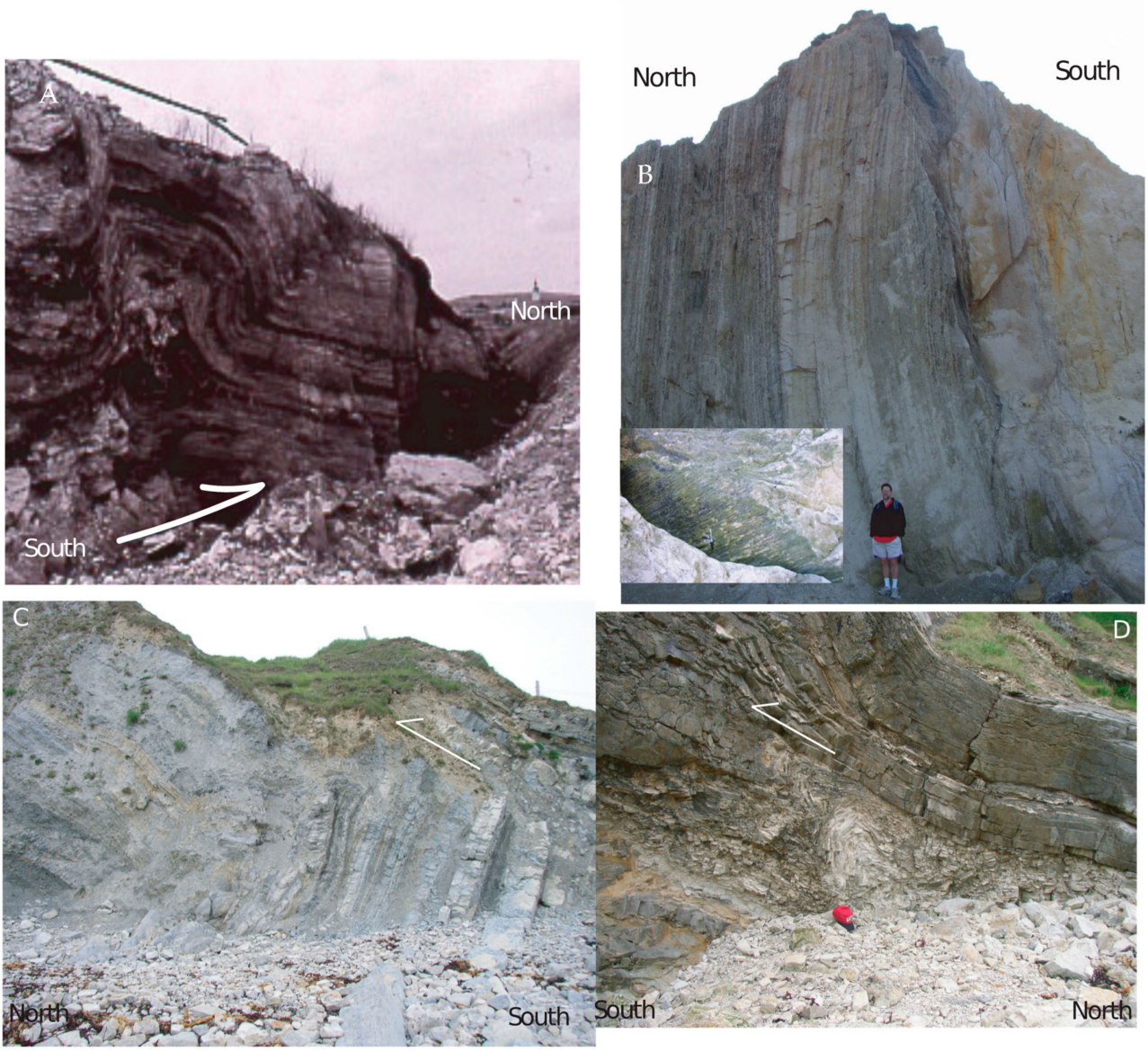

Figure 5. Field photos from the distal Alpine foreland. (**A**) Ramp anticline in Jurassic limestones and evaporites with a south-dipping thrust, Markt Nordheim, Germany. (**B**) Vertical Cretaceous limestones, Isle of Wight, UK, with inset of oblique-slip striations. (**C**,**D**) Thrust contraction structures in Jurassic limestones, Lulworth Cove, UK.

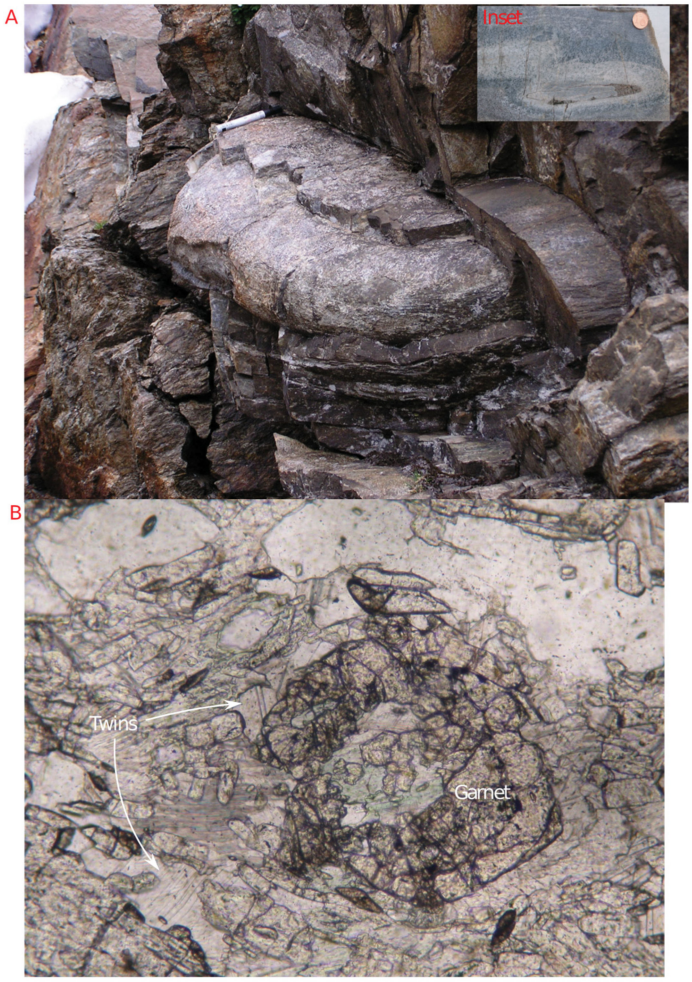

Figure 6. (**A**) Calcsilicate sheath folds in the Tauern window near Tyrol, Austria, including a section cut perpendicular to the fold axis (inset; penny for scale) and (**B**) photomicrograph of garnet (PL) surrounded by twinned calcite. Strain data in Tables 1 and 2.

4.3. Alpine Nappes and Molasse

Calcite strain data from the Alps are available from: the oldest, internal Helvetic–Penninic nappes ([40]; 29 samples), the Helvetic nappes ([73]; 14 samples plus 4 new strain results), the Helvetic flysch-molasse [41]; 20 samples], the Pre-Alps ([39]; 39 samples), the Molasse basin ([36,38]; 26 samples), and the youngest, frontal Jura folds ([36]; 9 samples, see also 37; Tables 1 and 2; Figures 7 and 8). Limestones in the Penninic nappes preserve a mix of LPS and LNS fabrics with no particular structural pattern. A comparison of e1 strain magnitudes reveals that the LNS twinning shortenings strains are higher (−7.5%) than the LPS shortening strains (−5.4%); these are the highest strain values due to the presence of thick twins [106]. The Helvetic nappes preserve a combination of layer-parallel and layer-normal shortening (sub-vertical) that is generally in the plane of tectonic transport, where the vertical shortening is associated with nappe stacking. We also analyzed four samples of fault-striated calcite from the Helvetic nappes, samples analyzed by Ring and Gerdes (2016) for U-Pb ages and fault kinematics; we find a horizontal shortening strain in the plane of nappe transport for calcite with U-Pb ages between 21.8 and 25.3 Ma. Shortening strains for the Helvetic LPS (−3.8%) and LPS (−3.98%) fabrics are comparable. The Pre-Alps (Penninic klippe) include 26 limestone samples and 13 calcite veins and a split of 20 LNS and 19 LPS fabrics with shortening and extension axes in no clear pattern. A comparison of e1 strain magnitudes reveals that the LNS twinning shortenings strains are higher (−5.81%) than the LPS shortening strains (−3.83%); this is expected, as the Pre-Alps are a continuation of the

Penninic nappes (Figure 3). The molasse sediments preserve a transport-parallel LPS fabric, as do the Jura limestones. Differential stress data are not available for all the study areas.

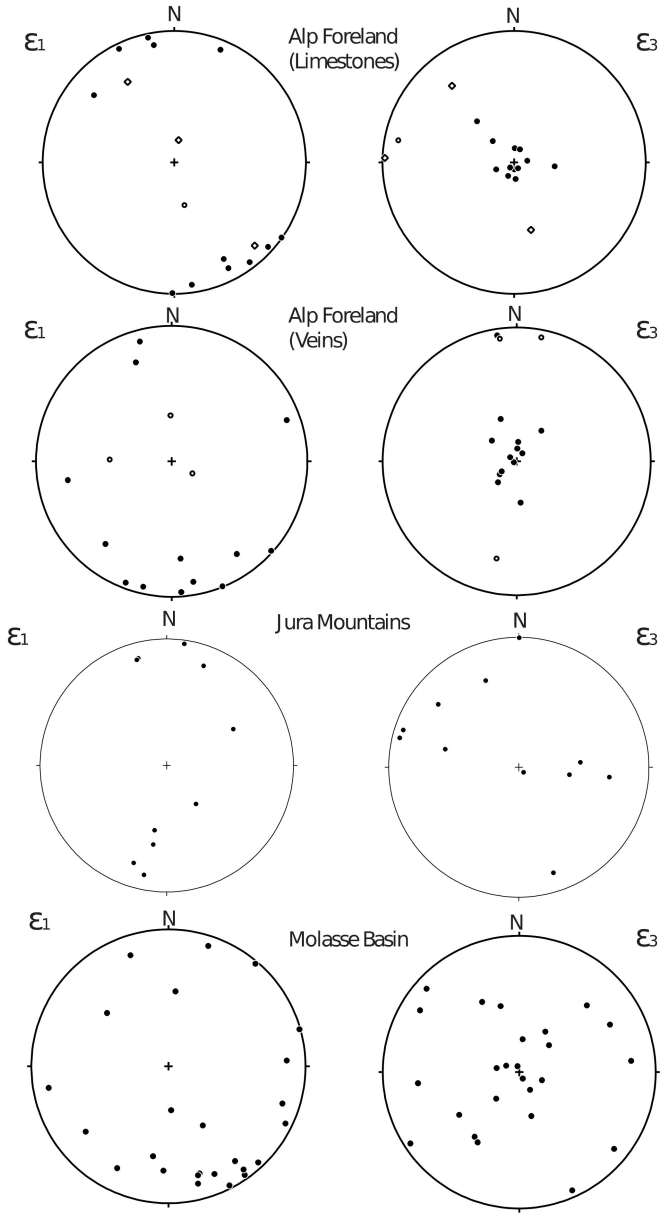

Figure 7. Lower hemisphere stereoplots of calcite strain data for the frontal Alps and foreland (e shortening axes; e3 = extension axes). Key: filled circles = LPS data; open circles = LNS fabric; open EV strain overprints. Strain data are in Tables 1 and 2 and field locations in Appendix A.

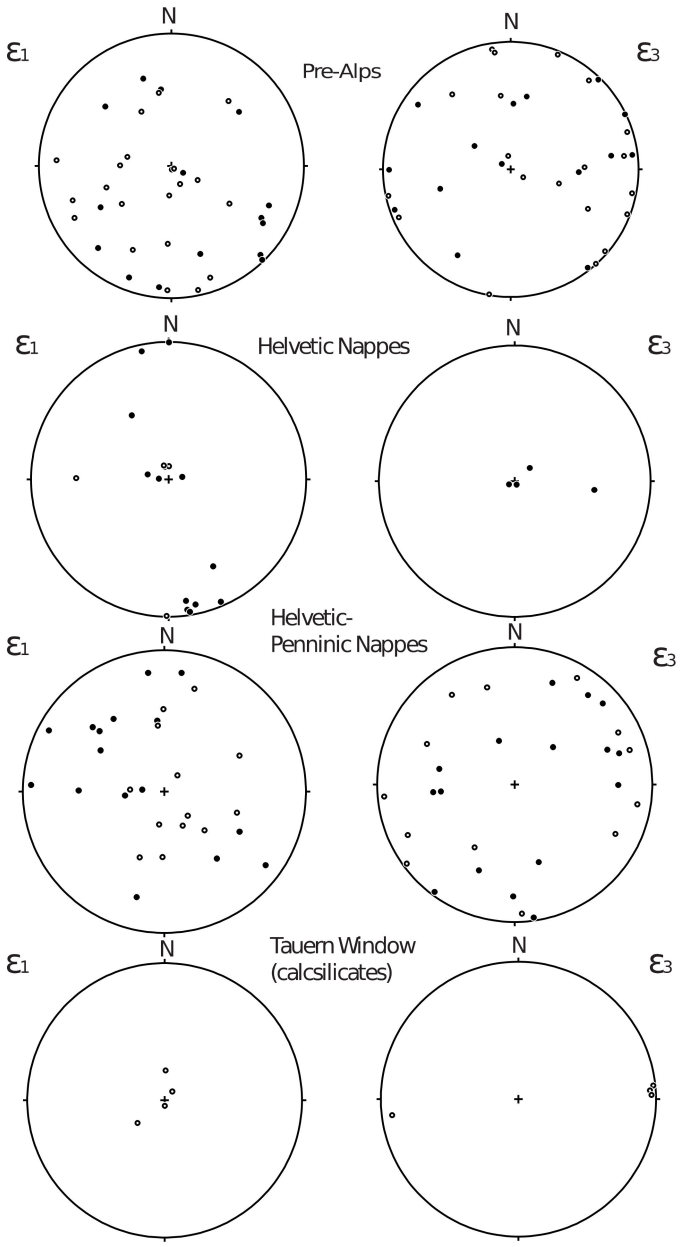

Figure 8. Lower hemisphere stereoplots of calcite strain data (e1 = shortening axes; e3 = extension axes) for different structural elements of the Alps. Key: filled circles are LPS fabrics, open circles are LNS fabrics.

4.4. Alpine Foreland

Alpine orogen strains are documented in the frontal Jura folds [37,41] and foreland in Burgundy [7,119]. We have expanded the foreland coverage 1000 km northwestward in the direction of Alpine tectonic transport and eastward across the French and German foreland (Figures 1 and 3) to document foreland deformation patterns and to see what role oroclinal bending played in the evolution of the Alps [41,71,120–123]. Thrust-related compressional structures are present far into the foreland, including northwest-facing ramp anticlines, southeast-verging back thrusts and some oblique faults (Figure 5; [124–126]). Limestones (12 samples, 15 strain analyses, n = 300 twin measurements) preserve a LPS fabric across the foreland adjacent to the Jura Mountains northwestward to the Cheddar Gorge–Bath area in Britain where Mesozoic outcrops become scarce (Figures 1 and 7; Tables 1 and 2). Six sample sites were combined into three strain analyses because of the small number of twins

and the closeness of sites to each other (Chatenois + Graux, Champlitte + N. Champlitte and Taxenne + Besancon, France). This resulted in PEV and NEV data splits, where the primary shortening strain recorded is SE-NW LPS with a sub-vertical shortening (NEV) overprint. In general, strain magnitudes are small and do not preserve any particular gradient across the region, although NEV percentages diminish away from the Alpine front. Foreland calcite veins along the southern British coast at Lulworth Cove and the Isle of Wight with U-Pb ages of ~34.7 Ma are in concert with an Alpine far-field origin (Parrish et al. 2017; these authors believe the deformation is Pyrenean). Calcite strain analyses in the foreland veins (17 samples, 19 strain analyses, n = 425 grains) reveal a SE-NW sub-horizontal shortening (15 results) and a NE-SW sub-vertical strain (4 results). Two samples allowed for a NEV split, one of which preserved a SE-NW LPS fabric and a vertical overprint (Grafenberg, Germany) while near Corfe Castle, Britain, two orthogonal sub-vertical strains are preserved. All four analyses from the Corfe site are from veins in a micritic Cretaceous limestone and are anomalous. Vein strain magnitudes are higher than strain magnitudes in the hosting limestones, while the inferred twinning differential stress magnitudes are regionally ~−350 bars. Vein fabrics are nearly even between VNS and VPS interpretations.

5. Discussion

The opening of the North Atlantic is preserved on the eastern margin of the ocean as Tertiary basalts in contact with Cretaceous chalks and limestones as a combination of sills, dikes and flows. Both the basalts and limestones are offset by numerous coast-parallel normal faults (with mm-scale offsets), rare normal fault hanging wall folds (i.e., Ballintoy Harbor; [127,128]) and numerous calcite veins. The extent of this field observation seems to be ~50 km inland from the margin, although this is also the distance where outcrops are dominated by the Welsh slate belt and an absence of Mesozoic sediments. Conversely, ~100 km southeastward from the Atlantic margin is also ~1000 km northwest of the Alps, and we observe a distinctive change in the outcrop-scale structures and calcite twinning strains preserved. The absence of the Alpine LPS fabric >1000 km can be explained by the existence of previously twinned and strain-hardened calcite near the older Atlantic margin, a decrease in the differential stress magnitude of the Alpine orogen to the northwest, or both. Summaries of twinning strain data, relative to distance from an active plate boundary, are presented in Figures 9 and 10. The Alpine foreland sites (Figures 9 and 10) record a mix of shortening strain magnitudes, which likely preserves a series of different orogenic events, namely the Pre-Alpine Pyrenean [14], the Alpine orogen and the active CRIS rift system [81,82].

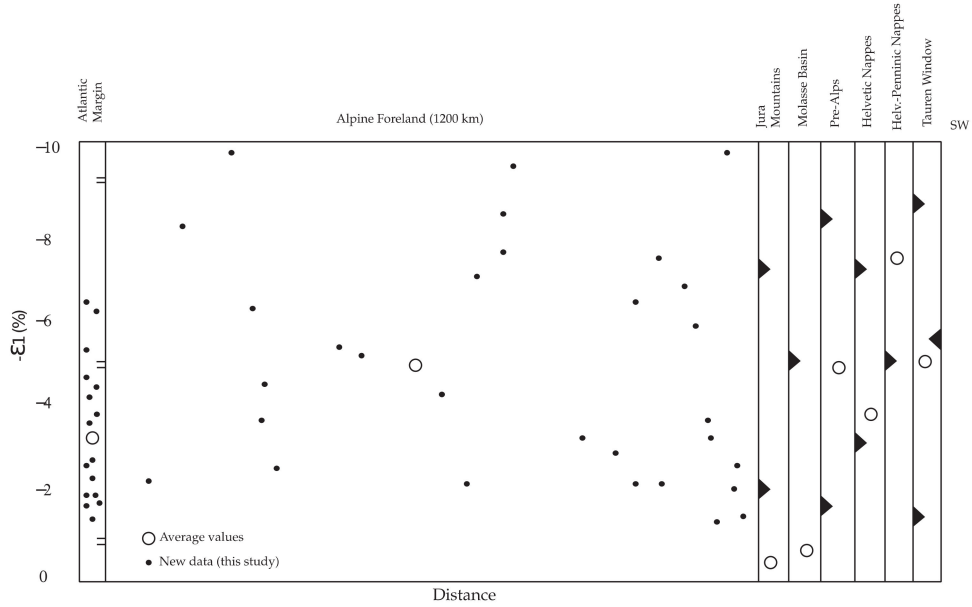

Figure 9. Plot of calcite twinning shortening strain (-e1) across the Alps, the Alpine foreland and the older (58 Ma) divergent Atlantic margin in Ireland.

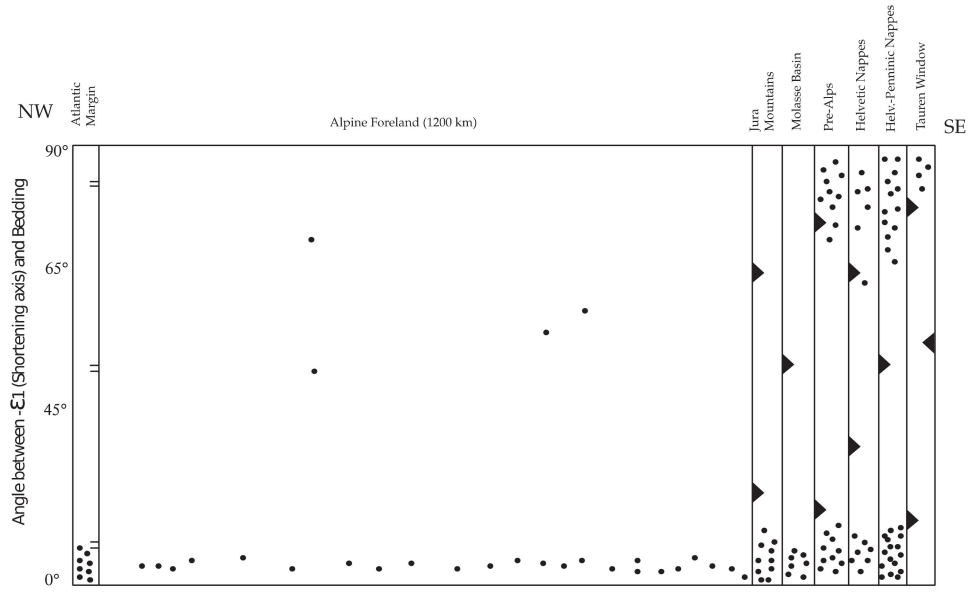

Figure 10. Plot of the angle between the calcite twining shortening axis and bedding for the Alps, Alpine foreland and the older (58 Ma) divergent Atlantic margin in Ireland.

5.1. Opening the Atlantic Ocean (Northern Irish Coast)

The calcite strains in Northern Ireland record a clean, consistent pattern of vertical extension and SW-NE sub-horizontal shortening. All the strains were measured in calcite veins or normal fault fillings that have a variety of orientations and cross-cut Tertiary basalts between the ages of 70–42 Ma (Figure 4). Curiously, the small-offset local structures and kinematics, sinistral striations on veins or stepped and striated calcite in normal faults have no relation to the stress–strain field of the regional setting. Evidence of a regional pattern is provided by the variability of the calcite vein orientations and dominance of VNS fabric interpretations; veins often preserve localized slip along their margins, which results in a VPS twinning strain. We interpret these results to indicate that vertical extension and margin-parallel sub-horizontal shortening dominated the evolution of the Irish portion of the Atlantic margin, where the margin-parallel horizontal differential stress was −350 bars

to a distance of ~50 km inboard from the current coast. Our results are consistent with and along strike of the Flamborough fault zone in northeastern Britain, where calcite fillings have U-Pb ages of 63–55 Ma [129]. Roberts and Walker [116] also report three sets of calcite-filled faults in the Faroe Islands with a range of U-Pb ages (44–11 Ma), and their set 3 fault kinematic interpretation (41.7 Ma) agrees with our margin-parallel shortening and margin-normal (SE-NW) extension twinning result. Our Irish strain pattern is distinctively different from the twinning strains along the active margin in Iceland, where ridge-normal sub-horizontal shortening (i.e., ridge-push; −480 bars) dominates with a ridge-parallel sub-vertical shortening overprint ([47]; see below). The Irish data (e1% and e1 angle vs. bedding) are plotted across the region to compare the Atlantic opening strain with younger Alpine deformation (Figures 9 and 10); margin-parallel shortening strains associated with opening the Atlantic margin are considerably higher than some parts of the frontal Alps.

5.2. The Alpine Nappes and Foreland Deformation

Our twinning strain data in the foreland, following the twinning paleostress work of Lacombe et al. [7,130] in the Alpine foreland, were intended to extend the sample coverage ~1000 km from the frontal Jura folds northwestward in the direction of tectonic transport and along strike to the northeast toward Nurnberg, Germany. This approach allowed us to document the distance of far-field Alpine tectonic stresses preserved by twinned calcite and the orientation of the Alpine stress–strain field northwest and north of the Central Alps. Our sample suite is dominated by calcite veins (n = 16) hosted in Mesozoic limestones (n = 13; Figures 1 and 5, Tables 1 and 2), and both suites preserve a SE-NW sub-horizontal shortening strain. The limestones record a layer-parallel shortening (LPS) fabric, and the veins are a nearly equal mix of VNS and VPS fabrics, with 15 results recording SE-NW horizontal shortening and 4 preserving NE-SW sub-vertical shortening (Figure 11A–C). The veins collected near Corfe Castle, Britain, record a complex sub-vertical twinning strain that is inconsistent with the remainder of the data (Figure 11, Tables 1 and 2). Strain overprints (high NEV%) are more common near the Alpine front, and the overprint includes one example of sub-vertical shortening (Figure 11) and a strain overprint parallel to the SE-NW Alpine shortening where the older, PEV twinning strain records N-S horizontal shortening (Iberia accretion, ECRIS extension?). The strain overprint complexities (Figures 9–11) in the Alpine foreland complement earlier calcite paleostress and outcrop fabric results of Lacombe et al. [7,130], where the persistent N-S horizontal shortening and compression are attributed to formation of the Pyrenees Mountains. Combining calcite twin studies with U-Pb ages on calcite veins and fault gouge would better resolve the timing and orientations of superimposed deformation events.

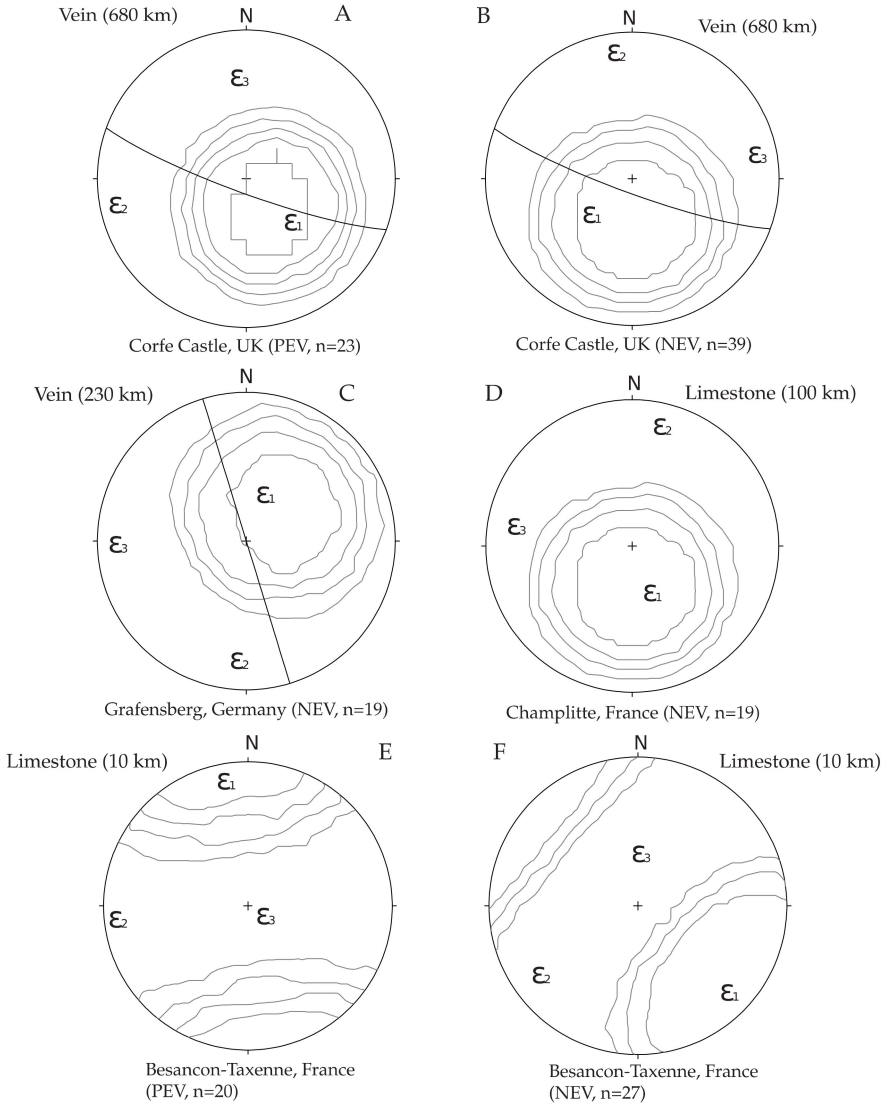

Figure 11. Stereoplots of calcite strain overprint (NEV) data that do not plot within the SE-NW plane of Alpine thrust transport and shortening (**A**–**D**) or of a twinning strain that does ((**E**,**F**); see Figure 1, Table 2). Key: e1 = shortening strain axis, e2 = intermediate axis, e3 = extension axis with Turner (1953) compression axes contoured. Great circles are veins.

Both the Mesozoic limestones and calcite veins (see Figure 11 for exceptions) preserve the same regional twinning fabric in marine sediments that are adjacent and autochthonous to the Alps, that is, sub-horizontal shortening parallel to the Alpine thrust transport direction. This strain is interpreted as a pre-thrusting strain imparted far into the foreland as an orogen evolved. This compares to the Appalachian collisional orogen, where the limestone and vein LPS fabric is parallel (SE-NW) in both the foreland and thrust belt [6,16,17]. In the Sevier belt in the western US, the LPS fabric in the foreland (E-W) is not parallel to the LPS fabric in the Idaho–Wyoming belt, which records a counterclockwise rotation of thrust sheets, from west to east, during the transpressive orogen [18–20].

Using our extended foreland data, we wanted to test this thrust sheet rotation hypothesis for the Alps, incorporating existing calcite twin strain results (Figures 1, 7 and 8). In structural order, from internal (SE) to external (NW): Variscan calcsilicates in the Tauern window contain abundant metamorphic calcite that preserves a distinctive sub-vertical shortening fabric as an Alpine-aged NEV data split and records burial by Helvetic–Penninic nappes [40]. Limestones in the Helvetic–Penninic nappes record a chaotic pattern of LPS and LNS fabrics that are not in the plane of Alpine tectonic transport. The Helvetic nappes

preserve a combination of layer-parallel and layer-normal shortening (sub-vertical) that is generally in the plane of tectonic transport, while the vertical shortening is associated with nappe stacking. The Pre-Alps preserve a complex pattern of LPS and LNS fabrics. The molasse sediments preserve a transport-parallel LPS fabric, as do the Jura limestones. A small subset of foreland veins preserve a variety of shortening axes oriented SW-NE with steep plunges and are not of Alpine origin (Figure 11; see [7,119]). There is parallelism between the LPS fabric e1 axes for the foreland limestones, veins, Jura folds, Molasse basin sediments and the Helvetic nappes, which suggests progressive tectonic transport of the Jura–Molasse–Helvetic structures in a constant northwest direction. The Pre-Alpine and Helvetic–Penninic strains are complex, suggesting non-plane strain deformation associated with nappe burial and thrust transport that were not everywhere toward the northwest (see [131,132]). Regional relations of shortening strains (e1%) and the angle between e1 and bedding are presented in Figures 9 and 10. Alpine nappes in Crete record a similar strain history with a LPS fabric in the nappes that is parallel to thrust transport, but the limestones and calcite veins in the synorogenic flysch preserve a complex, non-plane strain pattern [133,134].

5.3. Implications for Orogenic Collisions and Thrust Mechanics

The collision of Apulia into the European plate resulted in far-field translation of tectonic stresses and formation of contractional structures (Figures 3 and 5) and twinned calcite ~1200 km to the northwest of the Alps. Previously twinned calcite farther to the NW along the Atlantic margin strain hardened and did not preserve this new deformation with a twinning strain overprint, as all the NEV values are low (Table 2). The area of the critically tapered Alpine wedge includes the 1200 km of autochthonous foreland sediments and the Jura folds as well as the Helvetic and Penninic nappes. The latter have a width of 150 km, which, when palinspastically restored, augments to a width of 350 km [29,71] for a total pre-orogenic width of 1550 km. Thus, as a crude estimate, a total pre-orogenic width of 1550 km must be assumed for the initial Alpine wedge. The Alps formed by thrust shortening that progressed in time to the craton (NW), where the Molasse sediments and Jura-foreland sediments folded and cleaved at temperatures less than 100 °C, whereas the Alpine nappes are allochthonous, intensely deformed and metamorphosed with temperatures exceeding 300 °C [23,26,33,52–54,73,135].

During the early stages of orogenic convergence, horizontal tectonic stresses propagate into the foreland normal to the trench axis, thereby preserving a LPS twinning strain across the region; as shortening continued, the orientation of the pre-thrusting LPS fabric can be used to track motion of allochthonous rocks within the orogen. The SE-NW LPS fabric we observe in the Alpine foreland is parallel with the LPS fabric in the Jura and Helvetic allochthons, but the LPS fabric in the Molasse basin and the Helvetic–Penninic nappes is largely rotated out of the plane of thrust transport up to 90° (Figures 9 and 10) to accommodate the oroclinal shape and structure of the mountain belt. The Helvetic nappes acquired a secondary LNS twinning strain that is within the plane of thrust transport and is interpreted as a burial (vertical) shortening strain. Our strain data also indicate the Pre-Alp and Helvetic–Penninic nappes acquired a secondary LNS twinning strain during nappe formation and that thrust transport was out of the plane of thrust transport (Figure 8). As a collisional orogenic system, the Alps are unlike the collisional Appalachian [17], Grenville [19] or Mazatzal [136] orogens, because the hinterland indentor, the Adriatic margin of the Apulia plate, was actively deformed into the orogen and caused nappe formation, strain overprints and nappe motions out of the plane of tectonic transport. In contrast, Laramide crystalline uplifts in the Sevier belt foreland of Wyoming have oblique-slip kinematics, small fault offsets (<5 km) and no twinning strain overprint in hanging wall drape fold limestones [137].

The Alp foreland includes the rootless, concentric Jura folds, which changed into the low-amplitude, long-wavelength Paris basin, Purbeck monocline, Weald–Artois anticline and London basin to the north (Figure 1). These folds represent far-field Alpine

foreland deformation in the autochthonous footwall at a distance of ~1200 km, which is, not surprisingly, the same distance from the Alpine front where calcite is twinned (see [14]). For comparison, the Appalachian foreland includes sheared coal beds and salt-cored anticlines ~30 km inboard from the thrust front, the inversion Keweenaw–Kapuskasing thrust structure ~1220 km inboard [17] and twinned calcite in Paleozoic limestones >2000 km inboard. The Kiri uplift [138] in central Africa is ~4000 km inboard (south) and ~4000 km inboard (north) of the Caledonide and Cape orogenic belts, respectively, forming as Gondwana amalgamated in the Permian; basement inversion structures in the foreland are not part of the Alpine orogen. Orogenic forelands have different dimensions and different structural styles, including Taiwan fold belt (10 km foreland width), Zagros fold belt (300 km), Pyrenees (700 km), Alps (1200 km), Appalachian's (>2000 km) and Sevier belt (>2000 km; [9]). Deformation is related to plate convergence rates, thicknesses, slab dip (does an arc develop?) and the presence of pre-existing crustal weaknesses (i.e., Kiri uplift).

Our data set is a compilation of the results of many researchers (Table 2), so we do not have a complete view of twinning-related differential stresses. Our Alpine foreland data preserve a differential stress magnitude of −345 bars (−34.5 MPa), considerably lower than results presented by Lacombe et al. [130] of −55 to −88 MPa. Our results are consistent with the grand compilation of Beaudoin and Lacombe [10], namely −100 MPa at a normalized depth of 1 km.

5.4. Tectonic Evolution of the European Foreland (100–0 Ma)

The tectonic evolution of western Europe was a prolonged (~100 Ma) and complex process of accretion (Iberia), extension and shearing (sinistral opening of the Atlantic Ocean), collision of Apulia and subsequent ECRIS rifting [23,31,33,44–46,79,80,139,140]. Lacombe et al. [7,130] was the first to report calcite twinning paleostress data in a complex pattern in the Alpine foreland. Our anomalous foreland strain data (Figure 11) support Lacombe's results, which may be related to early, pre-Alpine N-S shortening Iberian accretion? [131,141,142], Pyrenees transpression, or post-Alpine extension (vertical shortening). A chronology of strain field data are presented in Figure 12: opening of the Atlantic Ocean (58 Ma) may have coincided with Iberian–Apulia collision as sinistral shearing dominated the Irish coast (Figure 4); the collision of the Adriatic margin of Apulia with Europe formed the Alps (starting at 100 Ma), with thrusting younging to the northwest [23]; we find calcite twinning strains are preserved ~1200 km into the foreland (Figures 7 and 8). Calcite previously twinned along the Irish Coast was strain-hardened and did not twin again. The modern tectonic shortening strain field is sub-horizontal, ~parallel to the Alpine field (NW-SE), dominated by shortening normal to the Atlantic margin in Iceland [47] and parallel to the strike of the Gubbio normal fault in Italy (NW-SE; 115 U-Pb calcite ages: 230,000 and 325,000 yr. BP) as Africa converges with Europe (see [143]).

Figure 12. Northwestern Europe with the Mid-Atlantic Ridge (orange line) defining the active divergent margin. Calcite twinning strain axes are presented by color (oldest to youngest): opening of the Atlantic Ocean (58 Ma; purple), and Alpine shortening (30 Ma, blue). Faroe Islands data from Roberts and Walker (2016) with Atlantic opening calcite ages ranging from 44–37 Ma. Flamborough Head preserves deformation ~63–55 Ma Roberts et al. [129]. Key: Colored lines represent layer-parallel shortening, circles are layer-normal shortening in the Alpine nappes (Table 2, Figures 7 and 8).

6. Conclusions

Mesozoic sediments in central Europe in the Alpine foreland preserve a complex array of calcite twinning strains associated with the collision of the Adriatic margin with Europe starting at 40 Ma. Twinning deformation is better preserved than by other brittle deformation markers [44,46,79,80] calcite vein and fault fillings (70–41 Ma U-Pb ages) in northern Ireland record a margin-parallel horizontal shortening strain with vertical extension up to ~100 km inboard (southeast) of the extensional Atlantic (58 Ma magnetic isochron) margin. The Alpine orogen (~50–5 Ma), along a traverse northwest from the Jura Mountains, is recorded by a thrust transport-parallel and horizontal shortening strain ~1200 km from the mountain front and includes thrusts and folds along the southern coast of Britain. Calcite strains become increasingly complex and bedding-normal (sub-vertical) toward the Alpine nappe stack in the Alps. Thrust sheet transport seems to be consistently normal (i.e., plane strain) to the strike of local thrust fault orientation except in the Helvetic–Penninic nappes (and Pre-Alp equivalents).

Author Contributions: J.P.C. conceptualization, writing, sampling and analysis, U.R. sampling and analysis, writing, O.A.P. analysis and writing. All authors have read and agreed to the published version of the manuscript.

Funding: This research received no external funding.

Acknowledgments: Martin Burkhard passed away in 2006, and this paper is a compilation of the efforts of many of his students and colleagues to honor his decades of inquiries in understanding the tectonics of the Alps. Martin and Adrian Pfiffner worked on understanding stress fields from fault kinematics and calcite twins with earthquake focal mechanisms [144]. Craddock and Burkhard spent time in the field in 2003, and our results were presented at the 2006 Geological Society of America meeting in Philadelphia in a session honoring Rick Groshong. Fieldwork for this study was undertaken during a sabbatical for Craddock in Erlangen, Germany, funded by the Mercator DFG program. Many of the authors participated in the foreland fieldwork, especially Cara Craddock and Jan Wood. Bernhard Schulz contributed the oriented Tauern samples and to our understanding of the complex geology in that portion of the Austrian Alps. Geochronology was conducted at the University of California, Santa Barbara, under the direction of Andrew Kylander-Clark.

Conflicts of Interest: The authors declare no conflict of interest.

Appendix A

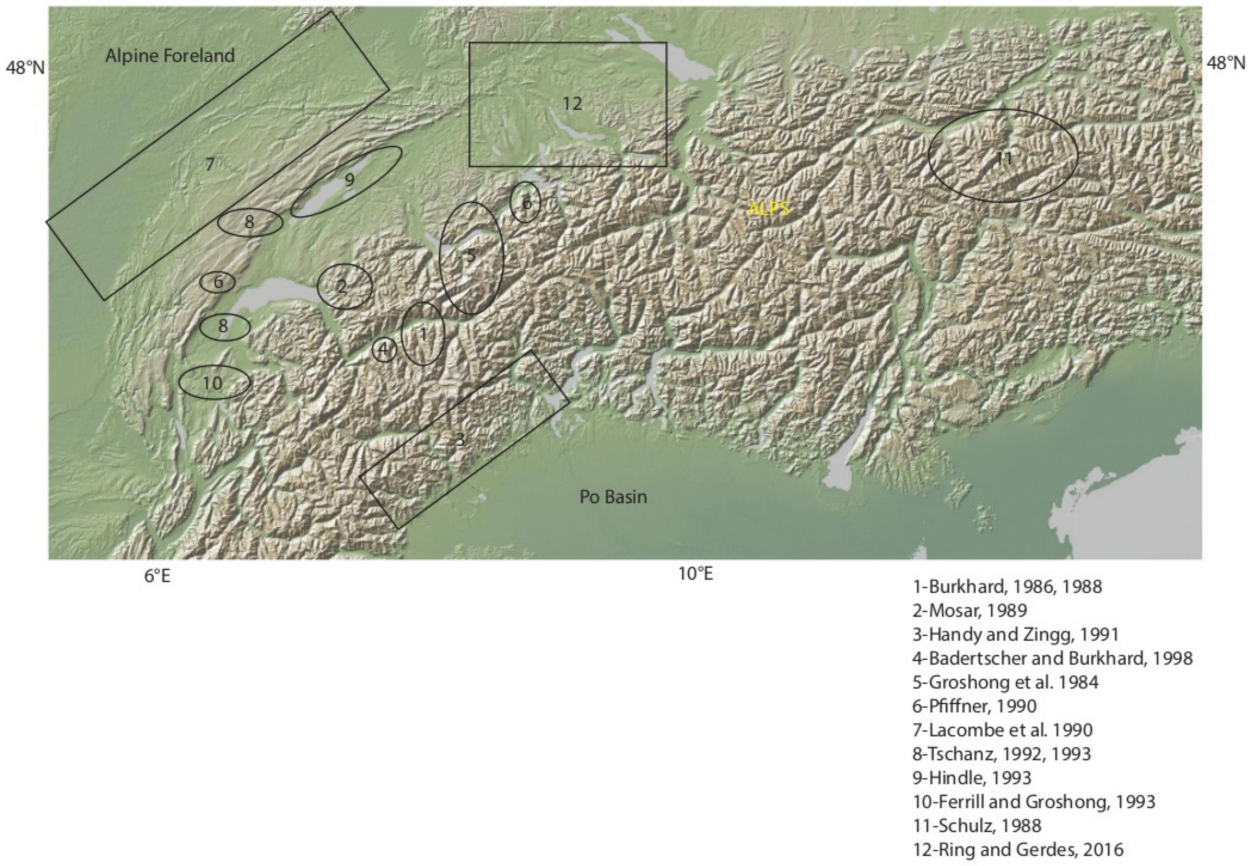

Figure A1. DEM of Alpine strain study locations.

Appendix B

Table A1. U-Pb calcite ages (Ireland).

Comments	U ppm	$^{238}U/^{206}Pb$	2σ	$^{207}Pb/^{206}Pb$	2σ	rho	Intercept Age	2σ
PUE21-44	0.008	2.86	0.70	0.809	0.023	0.03	76	153
PUE21-36	0.0004	0.40	0.45	0.890	0.025	0.03	−1177	1964
PUE21-13	0.005	0.90	0.83	0.871	0.029	−0.80	−326	639
PUE21-40	0.023	3.26	1.00	0.846	0.031	−0.36	−26	150
PUE21-34	0.018	4.04	2.79	0.824	0.032	−0.05	23	120
PUE21-31	0.026	5.28	2.05	0.806	0.033	−0.37	46	92
PUE21-7	0.011	0.84	0.96	0.826	0.033	0.37	93	585
PUE21-41	0.021	3.35	1.34	0.837	0.033	0.02	−3	147
PUE21-43	0.017	3.66	1.95	0.844	0.035	0.14	−19	138
PUE21-5	0.017	4.14	0.65	0.841	0.036	−0.06	−11	122
PUE21-30	0.038	13.03	2.76	0.772	0.041	−0.08	40	39
PUE21-22	0.013	3.91	1.44	0.792	0.043	−0.11	91	136
PUE21-47	0.025	8.95	1.85	0.784	0.046	−0.45	47	60
PUE21-25	0.008	1.63	0.88	0.864	0.048	0.62	−143	369
PUE21-28	0.013	7.24	4.34	0.769	0.049	0.06	75	87
PUE21-3	0.018	5.81	1.27	0.823	0.051	−0.39	18	99
PUE21-32	0.010	3.09	2.68	0.832	0.051	0.26	10	188
PUE21-9	0.010	0.73	0.82	0.869	0.051	0.47	−380	954
PUE21-46	0.009	3.01	1.85	0.852	0.054	0.82	−45	204
PUE21-19	0.004	0.65	1.12	0.860	0.054	−0.75	−311	1110
PUE21-35	0.004	0.38	0.40	0.808	0.057	−0.21	579	1647
PUE21-26	0.018	11.85	7.66	0.803	0.058	0.30	22	54
PUE21-29	0.020	9.69	2.17	0.777	0.059	−0.09	49	64
PUE21-49	0.007	16.52	11.17	0.810	0.064	0.42	13	41
PUE21-48	0.009	3.26	1.09	0.802	0.073	−0.46	84	218
PUE21-33	0.045	31.03	3.18	0.677	0.073	−0.05	42	22
PUE21-21	0.027	27.27	7.63	0.605	0.079	−0.08	69	32
PUE21-27	0.008	0.49	0.53	0.873	0.083	−0.38	−648	1913
PUE21-1	0.002	1.41	0.80	0.839	0.084	1.00	−20	565
PUE21-15	0.001	3.66	2.52	0.770	0.087	−0.25	145	238
PUE21-16	0.019	35.54	17.25	0.739	0.093	−0.84	22	26
PUE21-20	0.025	33.32	7.60	0.700	0.101	−0.69	33	28
PUE21-2	0.009	2.30	2.03	0.820	0.111	−0.05	55	432
PUE21-39	0.006	5.58	5.05	0.810	0.121	−0.64	37	193
PUE21-18	0.012	43.44	19.32	0.730	0.181	0.34	20	36
PUE21-11	0.006	6.90	4.87	0.950	0.191	0.51	−136	258
PUE21-17	0.008	10.66	10.66	0.840	0.231	0.31	−3	181
PUE21-38	0.007	31.70	26.56	0.810	0.280	−0.85	7	73
PUE23-37	0.056	53.80	7.73	0.435	0.053	0.29	61	12
PUE23-38	0.024	33.99	6.83	0.637	0.072	−0.17	48	22
PUE23-39	0.031	46.54	8.00	0.660	0.111	−0.73	31	21
PUE23-12	0.035	23.46	3.88	0.664	0.059	−0.36	60	26
PUE23-30	0.014	5.19	2.28	0.775	0.044	0.22	95	107
PUE23-1	0.045	6.48	1.01	0.794	0.030	0.09	52	71
PUE23-27	0.011	1.83	1.55	0.797	0.037	−0.12	171	299
PUE23-50	0.013	6.90	4.06	0.799	0.074	−0.28	43	107
PUE23-8	0.011	4.51	2.78	0.804	0.048	−0.05	57	127
PUE23-31	0.009	5.83	2.53	0.807	0.088	0.50	40	140
PUE23-28	0.031	11.17	1.93	0.809	0.060	0.42	19	56
PUE23-9	0.051	4.79	0.81	0.817	0.022	−0.03	32	91
PUE23-14	0.020	4.19	1.80	0.818	0.039	0.39	34	122

Table A1. *Cont.*

Comments	U ppm	$^{238}U/^{206}Pb$	2σ	$^{207}Pb/^{206}Pb$	2σ	rho	Intercept Age	2σ
PUE23-49	0.019	4.46	0.42	0.819	0.050	−0.34	30	127
PUE23-7	0.021	6.48	1.90	0.819	0.053	−0.46	21	91
PUE23-11	0.017	1.83	0.75	0.822	0.023	−0.23	60	241
PUE23-6	0.038	2.21	0.59	0.826	0.028	−0.59	35	209
PUE23-36	0.002	2.26	1.61	0.826	0.067	0.22	35	301
PUE23-44	0.004	7.33	5.04	0.840	0.131	−0.33	−5	156
PUE23-26	0.007	2.86	1.88	0.840	0.151	0.31	−13	455
PUE23-34	0.006	13.18	8.00	0.840	0.181	−0.72	−3	116
PUE23-20	0.005	2.86	1.33	0.848	0.082	0.49	−35	276
PUE23-32	0.007	5.19	2.11	0.850	0.151	−0.69	−23	251
PUE23-47	0.008	0.25	0.07	0.871	0.022	−0.54	−1247	2210
PUE23-19	0.010	4.89	2.24	0.872	0.100	0.08	−61	191
PUE23-29	0.033	0.18	0.03	0.884	0.018	−0.31	−2681	3809
PUE23-5	0.048	0.08	0.01	0.905	0.019	0.29	0	5882
PUE23-35	0.001	0.05	0.10	0.910	0.151	0.13	0	34,884
pue17-17	0.060	0.53	0.32	0.851	0.023	0.68	−239	893
pue17-25	0.056	2.30	1.80	0.600	0.240	0.68	806	1012
pue17-2	0.031	3.66	2.18	0.794	0.026	0.35	92	131
pue17-3	0.118	4.22	1.22	0.802	0.028	0.64	65	108
pue17-29	0.165	4.51	1.74	0.810	0.026	0.66	46	100
pue17-24	0.060	5.86	2.88	0.769	0.041	0.66	92	96
pue17-7	0.007	6.90	0.74	0.830	0.161	0.01	7	199
pue17-31	0.058	6.90	7.31	0.620	0.131	0.66	252	306
pue17-11	0.212	8.38	14.36	0.550	0.150	0.66	274	487
pue17-12	0.254	10.29	4.97	0.723	0.046	0.69	89	65
pue17-14	0.275	10.86	8.85	0.730	0.045	0.63	79	79
pue17-10	0.270	11.97	5.74	0.736	0.045	0.67	68	54
pue17-16	0.065	13.33	8.79	0.691	0.099	0.69	88	87
pue17-28	0.017	18.04	18.32	0.830	0.121	0.39	3	59
pue17-21	0.292	19.88	5.74	0.691	0.049	0.61	59	31
pue17-9	0.066	35.54	18.32	0.580	0.111	0.57	59	40
pue17-27	0.074	48.86	20.38	0.580	0.111	0.54	43	26
pue17-8	0.051	49.07	10.93	0.483	0.093	0.19	58	21
pue17-23	0.029	55.85	10.70	0.340	0.100	0.25	72	20
pue17-22	0.091	66.63	13.69	0.430	0.084	0.12	50	15
pue17-19	0.166	72.39	24.17	0.308	0.086	0.48	59	22
pue17-18	0.084	73.30	10.18	0.493	0.062	0.09	38	9
pue17-20	0.059	77.16	33.54	0.233	0.064	0.23	64	28
pue17-13	0.104	84.37	8.66	0.305	0.023	0.30	51	6
pue17-1	0.236	90.21	22.28	0.400	0.100	0.49	39	13
pue17-26	0.149	111.48	10.41	0.316	0.071	0.16	38	6
pue17-4	0.136	113.97	9.69	0.253	0.093	0.15	42	8
pue17-6	0.244	121.40	12.43	0.249	0.025	0.38	39	4
pue17-15	0.255	127.34	7.76	0.177	0.045	0.21	42	4
pue26-3	0.019	1.50	0.85	0.850	0.029	0.20	−78	323
pue26-5	0.001	1.70	1.45	0.807	0.062	0.01	136	390
pue26-6	0.011	4.69	4.88	0.816	0.086	0.04	34	174
pue26-8	0.082	23.74	4.16	0.694	0.042	0.33	49	22
pue26-9	0.044	14.48	13.23	0.583	0.059	0.36	141	134
pue26-10	0.064	15.64	2.52	0.715	0.050	0.41	63	35
pue26-11	0.021	15.43	9.95	0.760	0.131	0.26	40	77
pue26-12	0.054	11.97	3.06	0.801	0.046	0.62	24	45
pue26-13	0.032	4.34	1.93	0.778	0.057	0.27	108	145
pue26-15	0.002	12.09	11.10	0.870	0.141	0.01	−23	104
pue26-16	0.024	1.20	0.39	0.849	0.021	0.41	−92	381
pue26-17	0.041	3.55	1.72	0.833	0.051	0.28	6	163
pue26-18	0.018	17.00	5.43	0.730	0.121	0.13	51	63
pue26-19	0.021	3.35	1.06	0.871	0.066	0.06	−87	209

Table A1. *Cont.*

Comments	U ppm	$^{238}U/^{206}Pb$	2σ	$^{207}Pb/^{206}Pb$	2σ	rho	Intercept Age	2σ
pue26-21	0.012	6.01	0.90	0.859	0.065	0.11	−32	113
pue26-25	0.007	3.01	2.01	0.810	0.131	0.04	69	379
pue26-27	0.018	1.86	1.15	0.842	0.080	0.11	−28	416
pue26-28	0.076	68.58	14.90	0.265	0.095	0.22	68	19
pue26-29	0.037	1.17	1.64	0.812	0.028	0.23	163	446
pue26-30	0.039	4.51	0.77	0.830	0.030	0.30	10	105
pue26-31	0.010	1.30	2.32	0.771	0.099	0.44	397	956
pue26-32	0.019	5.10	4.21	0.580	0.150	0.45	401	403
pue26-34	0.073	6.44	1.18	0.794	0.025	0.32	53	68
pue26-35	0.127	8.56	1.63	0.791	0.026	0.30	42	52
pue26-37	0.076	0.88	0.23	0.857	0.020	0.19	−200	524
pue26-38	0.029	0.21	0.08	0.864	0.021	0.14	−1210	2633
pue26-39	0.024	3.66	3.09	0.817	0.098	0.15	41	246
pue26-40	0.056	0.34	0.28	0.800	0.121	0.09	812	2949
pue26-41	0.010	0.97	0.35	0.868	0.036	0.22	−277	561
ASH15-1	0.76	942.73	65.66	0.496	0.086	0.54	3	1
ASH15-1	0.82	1161.15	242.54	0.388	0.060	0.09	3	1
ASH15-10	1.59	1649.45	118.37	0.201	0.046	−0.01	3	0
ASH15-11	0.71	1714.56	105.97	0.082	0.059	0.17	4	0
ASH15-11	1.93	1719.59	111.34	0.251	0.087	0.18	3	0
ASH15-12	1.68	1411.26	78.29	0.304	0.059	0.29	3	0
ASH15-12	0.73	1633.37	205.08	0.264	0.051	0.60	3	0
ASH15-13	0.58	1670.59	223.83	0.310	0.160	0.57	3	1
ASH15-14	0.95	1651.77	114.22	0.256	0.069	0.10	3	0
ASH15-15	1.37	1804.24	95.87	0.194	0.049	−0.03	3	0
ASH15-16	0.96	1755.62	176.98	0.257	0.076	−0.15	3	0
ASH15-17	1.94	746.98	77.58	0.581	0.043	0.07	3	1
ASH15-18	0.50	1183.41	112.38	0.273	0.098	0.09	4	1
ASH15-19	1.24	1628.83	133.00	0.257	0.061	0.31	3	0
ASH15-2	0.01	11.73	11.73	0.860	0.860	0.04	−17	601
ASH15-2	0.65	1370.04	116.89	0.276	0.088	−0.17	3	1
ASH15-20	2.72	1742.58	92.28	0.185	0.014	0.41	3	0
ASH15-3	0.68	1274.74	195.65	0.320	0.110	0.03	3	1
ASH15-3	0.92	1719.59	177.34	0.270	0.170	0.16	3	1
ASH15-4	1.20	1224.17	64.86	0.470	0.110	0.28	2	1
ASH15-4	1.14	1873.41	139.79	0.181	0.068	0.31	3	0
ASH15-5	0.83	1412.96	149.11	0.362	0.056	−0.36	3	0
ASH15-5	1.75	1846.86	221.24	0.196	0.090	0.13	3	1
ASH15-6	1.98	1747.78	119.82	0.170	0.039	0.23	3	0
ASH15-6	1.02	1763.54	175.95	0.201	0.059	0.08	3	0
ASH15-7	1.03	747.93	37.90	0.543	0.051	0.22	3	1
ASH15-8	0.72	1758.26	91.39	0.306	0.069	0.11	2	0
ASH15-9	1.02	360.85	36.26	0.716	0.032	−0.37	3	1
ASH15-9	1.31	2008.15	206.82	0.192	0.076	0.20	3	0
db-1	18.00	64.51	2.99	0.282	0.009	0.04	70	4
db-1	26.20	68.26	2.10	0.267	0.008	0.51	68	3
db-10	17.61	57.57	3.03	0.301	0.011	−0.54	75	5
db-2	19.48	66.26	5.04	0.248	0.007	0.12	72	6
db-2	25.37	69.35	1.77	0.259	0.007	0.55	68	2
db-3	16.07	56.93	3.25	0.309	0.011	−0.74	75	5
db-3	20.71	61.08	4.01	0.316	0.020	0.15	69	6
db-4	10.08	44.42	3.00	0.418	0.017	−0.66	76	7
db-4	19.32	47.91	1.92	0.417	0.013	0.53	71	5
db-5	20.00	50.12	2.56	0.395	0.011	0.32	72	5
db-5	15.88	58.35	3.40	0.303	0.016	−0.70	74	5
db-6	22.70	65.37	3.13	0.284	0.011	0.32	69	4
db-6	16.33	65.89	3.93	0.260	0.007	−0.29	71	5
db-7	15.17	56.11	3.67	0.325	0.011	−0.65	74	6

Table A1. *Cont.*

Comments	U ppm	$^{238}U/^{206}Pb$	2σ	$^{207}Pb/^{206}Pb$	2σ	rho	Intercept Age	2σ
db-7	29.35	70.10	3.40	0.250	0.006	0.65	68	4
db-8	16.28	56.65	3.73	0.312	0.017	−0.54	75	6
db-8	34.60	73.16	3.02	0.254	0.006	0.59	65	3
db-9	18.03	65.41	2.97	0.256	0.006	0.32	72	4
WC1-1	3.78	21.80	1.56	0.109	0.007	−0.12	268	19
WC1-1	6.20	23.51	0.61	0.127	0.003	0.47	243	6
WC1-10	3.33	20.76	0.78	0.139	0.004	−0.33	270	10
WC1-2	4.02	20.08	2.95	0.130	0.041	−0.65	283	44
WC1-2	5.72	23.44	0.59	0.092	0.004	0.40	256	7
WC1-3	5.00	21.64	0.77	0.141	0.004	0.47	259	9
WC1-3	4.01	22.17	1.82	0.100	0.010	−0.55	267	22
WC1-4	4.15	23.22	2.75	0.094	0.002	−0.09	257	30
WC1-4	4.94	23.27	0.76	0.114	0.003	0.44	250	8
WC1-5	3.36	21.80	1.68	0.095	0.004	0.04	274	21
WC1-5	5.21	22.68	0.80	0.094	0.006	0.31	263	9
WC1-6	4.12	21.48	1.26	0.135	0.005	−0.14	263	15
WC1-6	6.54	21.80	0.85	0.141	0.009	0.14	257	11
WC1-7	4.03	21.28	1.31	0.117	0.003	−0.07	272	17
WC1-7	6.51	23.89	1.13	0.120	0.004	0.60	242	11
WC1-8	5.63	21.60	0.80	0.133	0.004	0.37	262	10
WC1-8	3.75	21.72	1.47	0.109	0.003	0.51	269	18
WC1-9	3.86	20.40	0.67	0.128	0.004	−0.27	279	9

References

1. Chinn, A.A.; Konig, R.H. Stress inferred from calcite twin lamellae in relation to regional structure of northwest Arkansas. *Geol. Soc. Am. Bull.* **1973**, *84*, 3731–3736. [CrossRef]
2. Nickelsen, R.P. Fossil distortion and penetrative rock deformation in the Appalachian plateau, Pennsylvania. *J. Geol.* **1966**, *74*, 924–931. [CrossRef]
3. Engelder, T.; Engelder, R. Fossil distortion and decollement tectonics of the Appalachian plateau. *Geology* **1977**, *5*, 457–460. [CrossRef]
4. Engelder, T.; Geiser, P. One the use of regional joint sets as trajectories of paleostress fields during the development of the Appalachian plateau, New York. *J. Geophys. Res.* **1980**, *85*, 6319–6341. [CrossRef]
5. Geiser, P.; Engelder, T. The distribution of layer-parallel shortening fabrics in the Appalachian foreland of New York and Pennsylvania: Evidence for two non-coaxial phases of the Alleghanian orogen. In *Contributions to the Tectonics and Geophysics of Mountain Chains*; Geological Society of America Memoirs: Boulder, CO, USA, 1983; Volume 158, pp. 161–176.
6. Craddock, J.P.; van der Pluijm, B.A. Late Paleozoic deformation of the cratonic carbonate cover of eastern North America. *Geology* **1989**, *17*, 416–419. [CrossRef]
7. Lacombe, O.; Angelier, J.; Laurent, P.; Bergerat, F.; Tourneret, C. Joint analyses of calcite twins and fault slips as a key for deciphering polyphase tectonics: Burgundy as a case study. *Tectonophysics* **1990**, *182*, 279–300. [CrossRef]
8. Lacombe, O.; Amrouch, K.; Mouthereau, F.; Dissez, L. Calcite twinning constraints on late Neogene stress patterns and deformation mechanisms in the active Zagros collision belt. *Geology* **2007**, *35*, 263–266. [CrossRef]
9. Lacombe, O. Calcite twins, a tool for tectonic studies in thrust belts and stable orogenic forelands. *Oil Gas Sci. Technol.* **2010**, *65*, 809–838. [CrossRef]
10. Beaudoin, N.; Lacombe, O. Recent and future trends in paleopiezometry in the diagenetic domain: Insights into the tectonic paleostress and burial depth history of fold-and-thrust belts and sedimentary basins. *J. Struct. Geol.* **2018**, *114*, 357–365. [CrossRef]
11. Chapple, W.M. Mechanics of thin-skinned fold-and-thrust belts. *Geol. Soc. Am. Bull.* **1978**, *89*, 1189–1198. [CrossRef]
12. Davis, D.; Suppe, J.; Dahlen, F.A. Mechanics of fold-and-thrust belts and accretionary wedges. *J. Geoph. Res.* **1983**, *88*, 1153–1172. [CrossRef]
13. Dahlen, F.A.; Suppe, J.; Davis, D. Mechanics of fold-and-thrust belts and Accretionary Wedges: Cohesive Coulomb theory. *J. Geophys. Res.* **1984**, *89*, 10087–10101. [CrossRef]
14. Lacombe, O.; Mouthereau, F. What is the real front of orogens? The Pyrenean orogen as a case study. *C.R. Acad. Sci. Ser. IIA Earth Planet. Sci.* **1999**, *329*, 889–896.
15. Wiltschko, D.V.; Medwedeff, D.A.; Millson, H.E. Distribution and mechanisms of strain within rocks on the northwest ramp of Pine Mountain block, southern Appalachian foreland: A field test of theory. *Geol. Soc. Am. Bull.* **1985**, *96*, 426–435. [CrossRef]
16. Kilsdonk, W.; Wiltschko, D.V. Deformation mechanisms in the southeastern ramp region of the Pine Mountain block, Tennessee. *Geol. Soc. Am. Bull.* **1988**, *100*, 644–653. [CrossRef]

17. Craddock, J.P.; Malone, D.H.; Porter, R.; Luczaj, J.; Konstantinou, A.; Day, J.E.; Johnston, S.T. Paleozoic reactivation structures in the Appalachian-Ouachita-Marathon foreland: Far-field deformation across Pangea. *Earth Sci. Rev.* **2017**, *169*, 1–34. [CrossRef]
18. Craddock, J.P. Transpression during tectonic evolution of the Idaho-Wyoming fold-and-thrust belt. *Reg. Geol. East. Ida. West. Wyo. Geol. Soc. Am. Mem.* **1992**, *179*, 125–139.
19. Craddock, J.P.; van der Pluijm, B.A. Regional stress-strain fields of Sevier-Laramide tectonism from calcite twinning data, west-central North America. *Tectonophys. Spec.* **1999**, *305*, 275–286. [CrossRef]
20. Craddock, J.P.; Malone, D.H. An overview of strains in the Sevier thin-skinned thrust belt, Idaho and Wyoming, USA (latitude 42° N). In *Tectonic Evolution of the Sevier-Laramide Hinterland, Thrust Belt, and Foreland, and Postorogenic Slab Rollback (180–20 Ma)*; Craddock, J.P., Malone, D.H., Foreman, B.Z., Konstantinou, A., Eds.; Geological Society of America: Boulder, CO, USA, 2021; Volume 555, pp. 133–148. [CrossRef]
21. Schmid, S.M.; Fugenschuh, B.; Kissling, E.; Schuster, R. Tectonic map and overall architecture of the Alpine orogen. *Eclogae Geol. Helv.* **2004**, *97*, 93–117. [CrossRef]
22. Rosenberg, C.L.; Kissling, E. Three-dimensional insight into Central-Alpine collision: Lower-plate or Upper-Plate indentation? *Geology* **2013**, *41*, 1219–1222. [CrossRef]
23. Pfiffner, O.A. *Geology of the Alps*; Wiley Publishers: Hoboken, NJ, USA, 2014; p. 392.
24. Price, J.B.; Wernicke, B.P.; Cosca, M.A.; Farley, K.A. Thermochronometry across the Austroalpine-Pennine boundary, Central Alps, Switzerland: Orogen—Perpendicular Normal Fault Slip on a Major "Overthrust" and its implications for orogenesis. *Tectonics* **2018**, *37*, 724–757. [CrossRef]
25. Schmid, S.M. The Glarus overthrust: Field evidence and mechanical model. *Eclogae Geol. Helv.* **1975**, *68*, 251–284.
26. Pfiffner, O.A.; Lehner, P.; Heitzmann, P.; Müller, S.; Steck, A. (Eds.) *Deep Structure of the Swiss Alps: Results of NRP 20*; Birkhäuser: Basel, Switzerland, 1997; pp. 101–114.
27. Pfiffner, O.A.; Schlunegger, F.; Buiter, S.J.H. The Swiss Alps and their peripheral foreland basin: Stratigraphic response to deep crustal processes. *Tectonics* **2002**, *21*, 1009. [CrossRef]
28. Kuhlemann, J.; Kempf, O. Post-Eocene evolution of the North Alpine Foreland Basin and its response to Alpine tectonics. *Sediment. Geol.* **2002**, *152*, 45–78. [CrossRef]
29. Burkhard, M.; Sommurga, A. Evolution of the western Swiss Molasse basin: Structural relations with the Alps and Jura belt: In Cenozoic Foreland Basins of Western Europe. *Geol. Soc. Spec. Publ.* **1998**, *134*, 279–298. [CrossRef]
30. Van der Pluijm, B.A.; Craddock, J.P.; Graham, B.R.; Harris, J.H. Paleostress in cratonic North America: Implications for deformation of continental interiors. *Science* **1997**, *277*, 792–796. [CrossRef]
31. Tavani, S.; Storti, F.; Lacombe, O.; Corradetti, A.; Munoz, J.A.; Mazzoli, S. A review of deformation pattern templates in foreland basin systems and fold-and-thrust belts: Implications for the stress in the frontal regions of thrust wedges. *Earth-Sci. Rev.* **2015**, *141*, 82–104. [CrossRef]
32. Lacombe, O.; Bellahsen, N. Thick-Skinned tectonics and basement-involved fold-thrust belts: Insight from selected Cenozoic orogens. *Geol. Mag.* **2016**, *153*, 763–810. [CrossRef]
33. Pfiffner, O.A. Thick-skinned and thin-skinned Tectonics: A global perspective. *Geosciences* **2017**, *7*, 71. [CrossRef]
34. Ring, U.; Bohar, R. Tilting, uplift volcanism and disintegration of the South German block. *Tectonophysics* **2020**, *795*, 228611. [CrossRef]
35. Craddock, J.P.; Burkhard, M. Alpine deformation from the internal Austrian Tauren window northwestward to the British foreland and Irish Tertiary province. *Geol. Soc. Am. Abstr. Programs* **2006**, *38*, 480.
36. Tschanz, X.; Sommaruga, A. Deformation associated with folding above frontal and oblique ramps around the rhomb-shaped Val-de-Ruz basin (Jura Mountains. *Ann. Tecton.* **1993**, *3*, 53–70.
37. Ferrill, D.A.; Groshong, R.H. Deformation conditions in the northern Subalpine chain, France, estimated from deformation modes in coarse-grain limestone. *J. Struct. Geol.* **1993**, *15*, 995–1006. [CrossRef]
38. Hindle, D. Quantifying Stresses and Strains from the Jura Arc, and Their Usefulness in Choosing a Deformation Model for the Region. Ph.D. Thesis, Neuchatel University, Neuchâtel, Switzerland, 1996.
39. Mosar, J. Internal deformation in the Prealpes Medianes, Switzerland. *Ecol. Geol. Helv.* **1989**, *82*, 765–793.
40. Burkhard, M. Deformation des calcaires de L'Helvetique de la Suisse occidentale (phenomènes, mécanismes et interprétations tectoniques). *Rev. Geol. Dyn. Geogr. Phys.* **1986**, *27*, 281–301.
41. Hindle, D.; Burkhard, M. Strain, displacement and rotation associated with the formation of curvature in fold belts: The example of the Jura arc. *J. Struct. Geol.* **1999**, *21*, 1089–1101. [CrossRef]
42. Groshong, R.H., Jr.; Teufel, L.W.; Gasteiger, C.M. Precision and accuracy of the calcite strain-gage technique. *Bull. Geol. Soc. Am.* **1984**, *95*, 357–363. [CrossRef]
43. Handy, M.R.; Zing, A. The tectonic and rheological evolution of an Attenuated cross section of the continental crust: Ivrea crustal section, southern Alps, northwestern Italy and southern Switzerland. *Geol. Soc. Am. Bull.* **1991**, *103*, 236–253. [CrossRef]
44. Kley, J.; Voigt, T. Late Cretaceous intraplate thrusting in central Europe: Effect of Africa-Iberia-Europe convergence, not Alpine collision. *Geology* **2008**, *36*, 839–842. [CrossRef]
45. Ring, U.; Gerdes, A. Kinematics of the Alpenrhein—Bodensee graben system in the Central Alps: Oligocene/Miocene transtension due to formation of the Western Alps arc. *Tectonics* **2016**, *35*, 1367–1391. [CrossRef]

46. Navabpour, P.; Malz, A.; Kley, J.; Sieburg, M.; Kasch, N.; Ustaszewski, K. Intraplate brittle deformation and states of paleostress constrained by fault kinematics in the central German platform. *Tectonophysiscs* **2017**, *694*, 146–163. [CrossRef]
47. Craddock, J.P.; Farris, D.; Roberson, A. Calcite-twinning constraints on stress-strain fields along the Mid-Atlantic Ridge, Iceland. *Geology* **2004**, *32*, 49–52. [CrossRef]
48. Dewey, J.F.; Helman, M.L.; Turco, E.; Hutton, D.H.W.; Knott, S.D. Alpine tectonics. In *Alpine Tectonics*; Coward, M.P., Dietrich, D., Park, R.G., Eds.; Special Publications; Geological Society: London, UK, 1989; Volume 45, pp. 265–283.
49. Platt, J.P.; Behrmann, J.H.; Cunningham, P.C.; Wallis, S.; Western, P.J. Kinematics of the Alpine arc and the motion history of Adria. *Nature* **1993**, *337*, 158–161. [CrossRef]
50. Ziegler, P.A.; Cloetingh, S.; van Wees, J.-D. Dynamics of intra-plate Compressional deformation: The Alpine foreland and other examples. *Tectonophysics* **1995**, *252*, 7–59. [CrossRef]
51. Frisch, W. The plate tectonic evolution of the Alps. *Tectonophysics* **1979**, *60*, 121–134. [CrossRef]
52. Escher, A.; Hunziker, J.C.; Marthaler, M.; Masson, H.; Sartori, M.; Steck, A. Geologic framework and structural evolution of the western Swiss-Italian Alps. In *Deep Structure of the Swiss Alps: Results of NRP 20*; Birkhauser: Basel, Switzerland, 1997; pp. 205–222.
53. Pfiffner, A.O.; Ellis, S.C.; Beaumont, C. Collisional tectonics in the Swiss Alps: Insights from geodynamic modeling. *Tectonics* **2000**, *19*, 1065–1094. [CrossRef]
54. Ring, U.; Brandon, M.T.; Ramthun, A. Soultion-mass-transfer deformation adjacent to the Glarus Thrust, with implications for the tectonic evolution of the Alpine wedge in eastern Switzerland. *J. Struct. Geol.* **2001**, *23*, 1491–1505. [CrossRef]
55. Carrapa, B. Tracing exhumation and orogenic wedge dynamics in the Alps via detrital thermochronology. *Geology* **2009**, *37*, 1127–1130. [CrossRef]
56. Carrapa, B.; DiGiulio, A.; Mancin, N.; Gupta, S.; Fantoni, R.; Stockli, D. Tectonic significance of Cenozoic deformation, exhumation and basin history in the Western Alps. *Tectonics* **2016**, *35*, 1892–1912. [CrossRef]
57. Mock, S.; von Hagke, C.; Schlunegger, F.; Dunkl, I.; Herwegh, M. Long-wavelength late Miocene thrusting in the north Alpine foreland: Implications for orogenic processes. *Solid Earth* **2020**, *11*, 1823–1847. [CrossRef]
58. Mancktelow, N.S. Neogene lateral extension during convergence in the Central Alps: Evidence from interrelated faulting and backfolding around Simplonpass (Switzerland). *Tectonophysics* **1992**, *215*, 295–317. [CrossRef]
59. Homewood, P.; Allen, P.A.; Williams, G.D. Dynamics of the Molasse Basin of Western Switzerland. In *Foreland Basins*; Special Publications of the International Association of Sedimentologists; Wiley Online Library: Hoboken, NJ, USA, 1986; Volume 8, pp. 199–217.
60. Schmid, S.M.; Pfiffner, O.A.; Schönborn, G.; Froitzheim, N.; Kissling, E. Integrated cross section and tectonic evolution of the Alps along the Eastern Traverse. In *Deep structure of the Swiss Alps: Results of NRP, 20*; Birkhauser Verlag: Basel, Switzerland, 1997; pp. 289–304.
61. Illies, J.H. Recent and paleo-intraplate tectonics in stable Europe and the Rhinegraben rift system. *Tectonophysics* **1975**, *29*, 251–264. [CrossRef]
62. Illies, J.H.; Greiner, G. Rhinegraben and the Alpine system. *Bull. Geol. Soc. Am.* **1978**, *85*, 770–782. [CrossRef]
63. Ziegler, P.A. Cenozoic rift of western and central Europe: An overview. *Geol. Mijnb.* **1994**, *73*, 99–127.
64. Platt, J.P. Dynamics of orogenic wedges and the uplift of high-pressure metamorphic rocks. *Geol. Soc. Am. Bull.* **1986**, *97*, 1037–1053. [CrossRef]
65. Royden, L.H. Evolution of retreating subduction boundaries formed during continental collision. *Tectonics* **1993**, *12*, 629–638. [CrossRef]
66. Wells, M.L.; Hoisch, T.D.; Cruz-Uribe, A.M.; Vervoort, J.D. Geodynamics of synconvergen extension and tectonic mode switching: Constraints from the Sevier-Laramide Orogen. *Tectonics* **2012**, *31*, TC1002. [CrossRef]
67. Molnar, P. Gravitational instability of mantle lithosphere and core complexes. *Tectonics* **2015**, *34*, 478–487. [CrossRef]
68. Siddans, A.W.B. Deformation, metamorphism and texture development in Permian mudstones of the Glarus Alps (eastern Switzerland). *Eclogae Geol. Helv.* **1979**, *72*, 601–621.
69. Ramsay, J.G. Tectonics of the Helvetic Nappes. In *Thrust and Nappe Tectonics*; The Geological Society of London: London, UK, 1981; pp. 293–309.
70. Ramsay, J.G.; Huber, M.I. *The Techniques of Modern Structural Geology, Volume 1: Strain Analysis*; Academic Press: Cambridge, MA, USA, 1983; p. 307.
71. Pfiffner, A.O. Kinematics and intrabed-strain in mesoscopically folded limestone layers: Examples from the Jura and Helvetic zone of the Alps. *Eclogae Geol. Helv.* **1990**, *83*, 585–602.
72. Badertscher, N.P.; Beaudoin, G.; Therrien, R.; Burkhard, M. Glarus overthrust: A major pathway for the escape of fluids out of the Alpine orogen. *Geology* **2002**, *30*, 875–878. [CrossRef]
73. Groshong, R.H.; Pfiffner, A.O.; Pringle, L.R. Strain partitioning in the Helvetic thrust belt of eastern Switzerland from leading edge to the internal zone. *J. Struct. Geol.* **1984**, *6*, 5–18. [CrossRef]
74. Kligfield, R.; Owens, W.H.; Lowrie, W. Magnetic susceptibility anisotropy, strain and progressive deformation in Permian sediments from the Maritime Alps (France). *Earth Planet. Sci. Lett.* **1981**, *55*, 181–189. [CrossRef]
75. Schmid, S.M.; Casey, M.; Starkey, J. The microfabric of calcite from the Helvetic nappes (Swiss Alps). In *Thrust and Nappe Tectonics*; McClay, K.R., Price, N.J., Eds.; Special Publications; Geological Society: London, UK, 1981; Volume 9, pp. 151–158.

76. Heitzmann, P. Calcite mylonites in the central alpine "root zone". *Tectonophysics* **1987**, *135*, 207–215. [CrossRef]
77. Marret, R.; Allmendinger, R.W. Kinematic analysis of fault-slip data. *J. Struct. Geol.* **1990**, *12*, 973–986. [CrossRef]
78. Allmendinger, R.W.; Cardozo, N.C.; Fisher, D. *Structural Geology Algorithms: Vectors & Tensors*; Cambridge University Press: Cambridge, UK, 2012; p. 289.
79. Rocher, M.; Cushing, M.; Lemeille, F.; Lozac'h, Y.; Angelier, J. Intraplate paleostresses reconstructed with calcite twinning and faulting: Improved method and application to the eastern Paris Basin (Lorraine, France). *Tectonophysics* **2004**, *387*, 1–21. [CrossRef]
80. Rocher, M.; Cushing, M.; Lemeille, F.; Baize, S. Stress induced by the Mio-Pliocene Alpine collision in northern France. *Bull. Soc. Géol. Fr.* **2005**, *176*, 319–328. [CrossRef]
81. Larroque, J.M.; Laurent, P. Evolution of the stress field pattern in the south Rhine Graben from the Eocene to the Present. *Tectonophysics* **1988**, *148*, 41–58. [CrossRef]
82. Lacombe, O.; Angelier, J.; Byrne, D.; Dupin, J.M. Eocene-Oligocene Tectonics and Kinematics of the Rhine-Saone Continental Transform Zone (Eastern France). *Tectonics* **1993**, *12*, 874–888. [CrossRef]
83. Groshong, R.H., Jr. Strain calculated from twinning in calcite. *Bull. Geol. Soc. Am.* **1972**, *83*, 2025–2038. [CrossRef]
84. Turner, F.J. Nature and dynamic interpretation of deformation lamellae in calcite of three marbles. *Am. J. Sci.* **1953**, *251*, 276–298. [CrossRef]
85. Turner, F.J. Compression and tension axes deduced from (0112) Twinning in calcite. *J. Geophys. Res.* **1962**, *67*, 1660.
86. Paulsen, T.S.; Wilson, T.J.; Demosthenous, C.; Millan, C.; Jarrad, R.; Laufer, A. Kinematics of the Neogene Terror rift: Constraints from calcite twinning strains in the ANDRILL McMurdo Ice Shelf (AND-1B) core, Victoria Land Basin, Antarctica. *Geosphere* **2014**, *10*, 828–841. [CrossRef]
87. Engelder, T. The nature of deformation within the outer limits of the central Appalachian foreland fold-and-thrust belt in New York state. *Tectonophysics* **1979**, *55*, 289–310. [CrossRef]
88. Spang, J.H.; Groshong, R.H., Jr. Deformation mechanisms and strain history of a minor fold from the Appalachian Valley and Ridge Province. *Tectonophysics* **1981**, *72*, 323–342. [CrossRef]
89. Groshong, R.H., Jr. Strain, fractures, and pressure solution in natural single-layer folds. *Bull. Geol. Soc. Am.* **1975**, *86*, 1363–1376. [CrossRef]
90. Groshong, R.H., Jr. Strain and pressure solution in the Martinsburg slate, Delaware Water Gap, New Jersey. *Am. J. Sci.* **1976**, *276*, 1131–1146. [CrossRef]
91. Ferrill, D.A. Calcite twin widths and intensities as metamorphic indicators in natural low-temperature deformation of limestone. *J. Struct. Geol.* **1991**, *13*, 675–677. [CrossRef]
92. Craddock, J.P.; Jackson, M.; van der Pluijm, B.A.; Versical, R. Regional shortening fabrics in eastern North America: Far-field stress transmission from the Appalachian–Ouachita orogenic belt. *Tectonics* **1993**, *12*, 257–264. [CrossRef]
93. Craddock, J.P.; Neilson, K.J.; Malone, D.H. Calcite twinning strain constraints on Heart Mountain detachment kinematics, Wyoming. *J. Struct. Geol.* **2000**, *22*, 983–991. [CrossRef]
94. Craddock, J.P.; McKiernan, A.; DeWit, M. Calcite twin analysis in synorogenic calcite, Cape Fold Belt: Implications for fold rotation and cleavage formation. *J. Struct. Geol.* **2007**, *27*, 1100–1113. [CrossRef]
95. Amrouch, K.; Lacombe, O.; Bellahsen, N.; Daniel, J.-M.; Callot, J.-P. Stress and strain patterns, kinematics and deformation mechanisms in a basement-cored anticline: Sheep Mountain Anticline, Wyoming. *Tectonics* **2010**, *29*, TC1005. [CrossRef]
96. Craddock, J.P.; Geary, J.; Malone, D.H. Vertical Injectites of Detachment Carbonate Ultracataclasite at White Mountain, Heart Mountain Detachment, Wyoming. *Geology* **2012**, *40*, 463–466. [CrossRef]
97. Craddock, J.P.; Craddock, S.D.; Konstantinou, A.; Kylander-Clark, A.; Malone, D.H. Calcite Twinning Strain Variations across the Proterozoic Grenville Orogen and Keweenaw-Kapuskasing Inverted Foreland, USA and Canada. *Geosci. Front.* **2017**, *8*, 1357–1384. [CrossRef]
98. Craddock, J.P.; Pearson, A. Non-coaxial horizontal shortening strains preserved in amygdule calcite, DSDP Hole 433C, Suiko Seamount. *J. Struct. Geol.* **1994**, *16*, 719–724. [CrossRef]
99. Craddock, J.P.; Pearson, A.; McGovern, M.; Kropf, E.P.; Moshoian, A.; Donnelly, K. Post-extension shortening strains preserved in calcites of the Keweenawan rift. In *Middle Proterozoic to Cambrian Rifting, Central North America*; Geological Society of America Special Paper, 213; Ojakgangas, R.W., Dickas, A.B., Green, J.C., Eds.; Springer: Dordrecht, The Netherlands, 1997; pp. 115–126.
100. Craddock, J.P.; Anziano, J.; Wirth, K.R.; Vervoort, J.D.; Singer, B.; Zhang, X. Structure, geochemistry and geochronology of a lamprophyre dike swarm, Archean Wawa terrane, Michigan, USA. *Precambrian Res.* **2007**, *157*, 50–70. [CrossRef]
101. Nuriel, P.; Weinberger, R.; Kylander-Clark, A.R.C.; Hacker, B.C.; Craddock, J.P. Calcite U-Pb ages constrain the evolution of the Dead Sea Fault. *Geology* **2017**, *45*, 587–590. [CrossRef]
102. Weinberger, R.; Nuriel, P.; Kylander-Clark, A.R.; Craddock, J.P. Temporal and spatial relations between large-scale fault systems: Evidence from the Sinai-Negev shear zone and the Dead Sea Fault. *Earth-Sci. Rev.* **2020**, *211*, 103377. [CrossRef]
103. Craddock, J.P.; Nuriel, P.; Kylander-Clark, A.R.; Hacker, B.R.; Luczaj, J.; Weinberger, R. Long-term (7 Ma) Strain Fluctuations within the Dead Sea Transform from High-resolution U-Pb Dating of a Calcite Vein. *Bulletin* **2022**, *134*, 1231–1246. [CrossRef]
104. Lacombe, O.; Parlangeau, C.; Beaudoin, N.; Amrouch, K. Calcite twin formation, measurement ad use as stress-strain indicators: A review of progress over the last decade. *Geosciences* **2021**, *11*, 445. [CrossRef]
105. Wenk, H.-R.; Takeshita, T.; Bechler, E.; Erskine, B.G.; Matthies, S. Pure Shear and Simple Shear Calcite Textures. Comparison of Experimental, Theoretical and Natural Data. *J. Struct. Geol.* **1987**, *9*, 731–745. [CrossRef]

106. Burkhard, M. Calcite twins, their geometry, appearance and significance as stress-strain markers and indicators of tectonic regime: A review. *J. Struct. Geol.* **1993**, *15*, 351–368. [CrossRef]
107. Lacombe, O.; Laurent, P. Determination of deviatoric stress tensors based on inversion of calcite twin data from experimentally deformed monophase samples: Preliminary results. *Tectonophysics* **1996**, *255*, 189–202. [CrossRef]
108. Ferrill, D.A. Critical re-evaluation of differential stress estimates from calcite twins in coarse-grained limestone. *Tectonophysics* **1998**, *285*, 77–86. [CrossRef]
109. Groshong, R.H., Jr. Experimental test of least-squares strain calculations using twinned calcite. *Bull. Geol. Soc. Am.* **1974**, *85*, 1855–1864. [CrossRef]
110. Rowe, K.J.; Rutter, E.H. Paleostress estimation using calcite twinning: Experimental calibration and application to nature. *J. Struct. Geol.* **1990**, *12*, 1–17. [CrossRef]
111. Teufel, L.W. Strain analysis of experimental superposed deformation using Calcite twin lamellae. *Tectonophysics* **1980**, *65*, 291–309. [CrossRef]
112. Evans, M.A.; Groshong, R.H. A Computer Program for the Calcite Strain-Gage Technique. *J. Struct. Geol.* **1994**, *16*, 277–281. [CrossRef]
113. Ferrill, D.A.; Morris, A.P.; Evans, M.A.; Burkhard, M.; Groshong, R.H.; Onasch, C.M. Calcite Twin Morphology: A Low-Temperature Deformation Geothermometer. *J. Struct. Geol.* **2004**, *26*, 1521–1529. [CrossRef]
114. Gray, M.B.; Stamatakos, J.A.; Ferrill, D.A.; Evans, M.A. Fault-Zone Deformation in Welded Tuffs at Yucca Mountain, Nevada, USA. *J. Struct. Geol.* **2005**, *27*, 1873–1891. [CrossRef]
115. Craddock, J.P.; Malone, D.H.; Wartman, J.; Kelly, M.J.; LJunlai, L.; Bussolotto, M.; Invernizzi, C.; Knott, J.; Porter, R. Calcite Twinning Strains from Syn-faulting Calcite Gouge: Small-Offset Strike-Slip, Normal and Thrust Faults. *Int. J. Earth Sci.* **2020**, *109*, 1–42. [CrossRef]
116. Roberts, N.M.W.; Walker, R.J. U-Pb geochronology of calcite-mineralized faults: Absolute timing of rift-related fault events on the northeast Atlantic margin. *Geology* **2016**, *44*, 531–534. [CrossRef]
117. Schulz, B. Deformation, Metamorphose and Petrographie im Ostalpinen Altkristallin Sudlich des Taurenfensters. Ph.D. Thesis, University of Erlangen-Nuremberg, Erlangen, Germany, 1988; p. 133.
118. Rosenberg, C.L.; Brun, J.-P.; Gapais, D. Indentation model of the eastern Alps and the origin of the Tauren Window. *Geology* **2004**, *32*, 997–1000. [CrossRef]
119. Lacombe, O.; Angelier, J.; Laurent, P. Determining paleostress orientations from faults and calcite twins: A case study near the Sainte-Victoire Range (southern France). *Tectonophysics* **1992**, *201*, 141–156. [CrossRef]
120. Burkhard, M. Aspects of large-scale Miocene deformation in the external part of the Swiss Alps (Subalpine Molasse to Jura fold belt). *Eclogae Geol. Helv.* **1990**, *83*, 559–583.
121. Homberg, C.; Hu, J.C.; Angelier, J.; Bergerat, F.; Lacombe, O. Characterization of stress perturbations near major fault zones: Insights from 2-D distinct-element numerical modeling and field studies (Jura Mountains). *J. Struct. Geol.* **1997**, *19*, 703–718. [CrossRef]
122. Becker, A. In Situ stress data from the Jura Mountains-new results and interpretation. *Terra Nova* **1999**, *11*, 9–15. [CrossRef]
123. Homberg, C.; Lacombe, O.; Angelier, J.; Begerat, F. New constraints for indentation mechanisms in arcuate belts from the Jura Mountains, France. *Geology* **1999**, *27*, 827–830. [CrossRef]
124. House, M.R. The Structure of Weymouth Anticline. *Proc. Geol. Assoc.* **1961**, *72*, 211–238. [CrossRef]
125. House, M.R. *Geology of the Dorset Coast. Geologists' Association Guide, 22*; Geologists' Association: London, UK, 1986.
126. Sanderson, D.J.; Dix, J.K.; Westhead, K.R.; Collier, J.S. Bathymetric mapping of the coastal and offshore geology and structure of the Jurassic Coast, Weymouth Bay, UK. *J. Geol. Soc. Lond.* **2017**, *174*, 498–508. [CrossRef]
127. Lyle, P. *A Geological Excursion Guide to the Giant's Causeway*; Baird Publishers: London, UK, 1998; ISBN 0-9528258-1-3.
128. Lyle, P. *The North of Ireland*; Terra Publishing: Arnhem, The Netherlands, 2003; ISBN 1-903544-08-4.
129. Roberts, N.M.W.; Lee, J.K.; Holdsworth, R.E.; Jeans, C.; Farrant, A.R.; Haslam, R. Near-surface Palaeocene fluid flow, mineralisation and faulting at Flamborough Head, UK: New field observations and U-Pb calcite dating constraints. *Solid Earth* **2020**, *11*, 1931–1945. [CrossRef]
130. Lacombe, O.; Laurent, P.; Angelier, J. Calcite twins as a key to paleostresses in sedimentary basins: Preliminary results from drill cores of the Paris basin. In *Peri-Tethyan Platforms*; Roure, F., Ed.; Technip: Paris, France, 1994; pp. 197–210.
131. Ratschbacher, L. Kinematics of Austro-Alpine cover nappes: Changing translation path due to transpression. *Tectonophysics* **1986**, *125*, 335–356. [CrossRef]
132. Beltrando, M.; Lister, G.; Hermann, J.; Forster, M.; Compagnoni, R. Deformation mode switches in the Penninic units of the Urtier Valley (Western Alps): Evidence for a dynamic orogen. *J. Struct. Geol.* **2008**, *30*, 194–219. [CrossRef]
133. Craddock, J.P.; Klein, T.; Kowalczyk, G.; Zulauf, G. Calcite twinning strains in Alpine orogen flysch: Implications for thrust-nappe mechanics and the geodynamics of Crete. *Lithosphere* **2009**, *1*, 174–191. [CrossRef]
134. Klein, T.; Craddock, J.P.; Zulauf, G. Constraints on the geodynamical evolution of Crete: Insights from illite crystallinity, Raman spectroscopy and calcite twinning above and below the "Cretan detachment". *Int. J. Earth Sci.* **2013**, *102*, 139–182. [CrossRef]
135. Burkhard, M. L'Helvétique de la bordure occidentale du massif de l'Aar (évoltion tectonique et métamorphique). *Eclogae Geol. Helv.* **1988**, *81*, 63–114.

136. Craddock, J.P.; McKiernan, A.W. Tectonic implications of finite strain gradient in Baraboo-interval quartzites (ca. 1700 Ma), Mazatzal orogen, Wisconsin and Minnesota, USA. *Precambrian Res.* **2007**, *156*, 175–194. [CrossRef]
137. Craddock, J.P.; Malone, D.H.; Konstantinou, A.; Spruell, J.; Porter, R. Calcite twinning strains associated with Laramide uplifts, Wyoming Province. In *Tectonic Evolution of the Sevier-Laramide Hinterland, Thrust Belt, and Foreland, and Postorogenic Slab Rollback (180–20 Ma)*; Special Paper 555; Craddock, J.P., Malone, D.H., Foreman, B.Z., Konstantinou, A., Eds.; Geological Society of America: Boulder, CO, USA, 2022; pp. 149–192. [CrossRef]
138. Daly, M.C.; Lawrence, S.R.; Kimun'a, D.; Binga, M. Late Paleozoic deformation in central Africa: A result of distant collision? *Nature* **1991**, *350*, 605–607. [CrossRef]
139. Stampfli, G.M.; Hochard, C. *Plate Tectonics of the Alpine Realm: Ancient Orogens and Modern Analogues*; The Geological Society of London: London, UK, 2009; Volume 327, pp. 89–111.
140. Le Breton, E.; Handy, M.R.; Molli, G.; Ustaszewski, K. Post-20 Ma motion of the Adriatic plate: New constraints from surrounding Orogens and implications for crust-mantle decoupling. *Tectonics* **2017**, *36*, 3135–3154. [CrossRef]
141. Ring, U.; Ratschbacher, L.; Frisch, W.; Biehler, D.; Kralik, M. Kinematics of the Alpine plate margin: Structural styles, strain and motion along the Penninic-Austroalpine boundary in the Swiss-Austrian Alps. *J. Geol. Soc. Lond.* **1989**, *146*, 835–849. [CrossRef]
142. Neubauer, F.; Genser, J.; Handler, R. The Eastern Alps: Result of a two-stage collision process. *Mitt. Osterr. Geol. Ges.* **1999**, *92*, 117–134.
143. Howe, T.C.; Bird, P. Exploratory models of long-term crustal flow and resulting seismicity in the Alpine-Aegean orogen. *Tectonics* **2010**, *29*, TC4023. [CrossRef]
144. Pfiffner, O.A.; Burkhard, M. Determination of paleo-stress axes Orientations from fault, twin and earthquake data. *Ann. Tecton.* **1987**, *1*, 48–57.